Frame-invariant modeling for non-Brownian suspension flows

Ayoub Badia, Yves D'angelo, François Peters, Laurent Lobry

Frame-invariant modeling for non-Brownian suspension flows

Ayoub Badia[a,b], Yves D'Angelo[a], François Peters[b], Laurent Lobry[b]

[a] *Université Côte d'Azur, Laboratoire Mathématiques & Interactions J A Dieudonné, LJAD, UMR 7351 CNRS, Nice, France*
[b] *Université Côte d'Azur, Institut de Physique de Nice, InPhyNi, UMR 7010 CNRS, Nice, France*

Abstract

In this paper, we present a continuum modeling for three-dimensional flows of non-colloidal, non-Brownian suspensions of particles immersed in a Newtonian liquid. Such suspensions exhibit complex behaviors such as jamming, anisotropic normal stresses and shear-induced particle migration. These non-Newtonian effects arise from the solid contact forces between the particles when the suspension is sufficiently concentrated. The modeling consists of a macroscopic one-phase model close to the "Suspension Balance Model" [1, 2, 3, 4]. The particles migration flux is governed by the divergence of the contact stresses tensor. In order to describe the flow in general 3D geometries, a frame-invariant constitutive law for the stresses in flowing suspensions is developed. It is similar to the second-order fluid modeling, which is well-known in polymer rheology, and allows for the presence of anisotropic normal stresses. The material functions are deduced from discrete simulation data from the literature. The behavior of the model in shear and extensional flows is discussed, as well as its limitations when used for a more general flow. To assess the modeling, numerical computations are performed using a finite volume method from the OpenFOAM suite. The implementation of the modeling is first validated by studying particles migration in some classical rheometric flows and then by studying the complex flow of a suspension in a tube through an abrupt expansion.

1. Introduction

Understanding particulate suspension flows is of primary interest in a wide range of applications, spanning from natural flows (blood flow, lavas or debris flows) to industrial processes (fresh concrete manipulation, food processing, paint coating). A large amount of literature has been devoted to suspension flows, that not only evidenced the great complexity of such materials, but also provided keys to understand their properties (see [5] for a recent review). Non-Brownian suspensions display many complex rheological behaviors, such as shear-thinning [6, 7, 8], continuous and discontinuous shear-thickening (see [9] for a review) and anisotropic normal stresses [10]. Time-varying suspension flows may also display more peculiar features, such as stress discontinuity at shear-reversal [6, 11, 12] and strain amplitude dependent response in oscillatory shear flow [13, 14]. Particles in suspension flows undergo shear-induced migration [15, 16], sedimentation, resuspension [17, 18, 19]. At particle scale, relevant mechanisms are hydrodynamic interactions together with direct contact interactions resulting in shear-induced microstructure [20, 21, 22] and irreversibility [23].

During the last decades, particle scale simulations have allowed deep insight in the microscopic mechanisms responsible for the suspensions flow behaviors (see [24] for a review), highlighting first the influence of lubrication interactions and shear-induced microstructure [25, 26] and later the role of contact between particles [27, 28] in suspension rheology. However, even though more and more powerful computers become available, discrete simulations are mainly restricted to moderately large systems invol-

ving a few thousand up to tens of thousands particles. While such simulations are well suited to determine material functions in homogeneous suspensions, they do not allow one to tackle real flows in complex geometries. Continuum modeling can then appear as an interesting modeling strategy. Such models dealing with suspension flows and particle transport may be categorized in two main classes. In the frame of the first class, the so-called "two-phase" or "two-fluid" model, the particle and liquid phases are modeled as two interpenetrating and interacting continuums, each with its own volume fraction and velocity field. Each phase obeys mass and momentum conservation equations (energy conservation equation may be added, if needed), and the phases interact with each other due to mass and momentum (and possibly energy) transfer. Part of these equations may be deduced from fundamental balance equations at particle scale [29], but some closure relations have to be stated on an experimental basis or from theoretical conjectures. In the case of incompressible, non-reacting, athermal suspensions, such models deal with at least 8 scalar fields, say the solid volume fraction, the pressure and two vector velocity fields. Such models are naturally well-suited to flows where the two phases move with significantly different velocities as in the case of fluidized beds [30] or bed-load transport [31]. This is however at the cost of computational difficulties, since a quite large number of coupled fields must be computed.

Another class of models mainly considers the flow of the mixture as a whole, together with a balance equation for the solid volume fraction. The latter involves a specific flux that accounts for the motion of the particle phase with respect to the mixture. This flux may be written as an athermal diffusive flux depending on the volume fraction gradient and on the shear-rate gradient [32]. Other models start from the particle phase momentum equation mentioned in the previous paragraph and after some algebraic manipulation derive the expression of the drift velocity, i.e. the velocity of the particle phase with respect to the mixture. The resulting flux is given mainly as a function of the divergence of some particle stress tensor, which expression has to be stated as an additional closure relationship. Such models are usually referred to the "Suspension Balance Model" [1, 2, 3, 4]. In the present paper, we follow this approach, as explained in 2.1. Such models are computationally less expensive than two-fluid models, since only 5 scalar fields have to be determined. They are well-suited to problems where the particle phase velocity is close to the liquid velocity.

Constitutive relations must be stated, that allow computation of the relevant stresses (suspension stress, particle stress). Different types of such relation have been proposed in the literature. Most of the experimental or simulation data deal with simple shear flows, so that stresses have first been written in a vector basis corresponding respectively to the flow, velocity gradient and vorticity directions, that is well-suited to rheometrical shear flows [3]. The aforementioned model accounts for the suspension viscosity, and anisotropic normal stresses, both depending on the particle volume fraction ϕ, and proportional to the shear rate $\dot{\gamma}$. We note here that in the last decade, pressure imposed shear flow experiments have led to an alternative but equivalent form of the material functions, where the stresses are written as a function of the particle pressure P_p and the viscous number $J = \frac{\eta_f \dot{\gamma}}{P_p}$ [33, 5, 34]. The main drawback of the model of [3] is that it is restricted to simple shear flow and thus cannot tackle general flow geometries. It should be noted however that a frame-invariant generalization of this model has been proposed for two-dimensional flows [35]. In addition, the aforementioned model is restricted to steady flows and cannot account for the specific behaviors of the suspensions in time varying flows, such as oscillatory flows or shear-reversal.

More general models have been proposed, that explicitly account for the influence of the so-called shear-induced microstructure, i.e. the local relative arrangement of the particles, on stresses (see the reviews in refs. [36, 37] and

recent works in this area [38, 39, 40, 41]). This microstructure is usually modeled using one or more tensor fields, which obey a time differential equation, and a constitutive relation that connects the stress and the microstructure must be stated. Such models are very attractive since they stick to the particle scale sound concept of microstructure. They allow in principle to tackle any steady or transient flow geometry, from extensional to purely rotational flows, and may be in quite fair agreement with experimental data [42, 40]. However, they are not that simple to tackle : finding a mathematical object that would properly describe the microstructure as measured in discrete simulations is not an easy task [38]. In addition, they usually involve a quite large number of free parameters, that should be determined from experiments or discrete simulations dealing with relevant flows, in particular transient non-shear flows. Even though considerable effort to generate such data [43, 38, 44] has been carried out, calibration of aforementioned modeling remains a quite difficult task.

In the present paper, we follow a simplified approach, with no explicit reference to microstructure modeling. We propose a frame-invariant constitutive relation that allows computation of the relevant stresses in nearly steady flows. Such modeling is not suited to flow geometries where flow conditions as seen by the moving fluid undergo rapid changes. In particular, fast transient flows like shear-reversal or oscillatory flows are not expected to be properly accounted for. However, such models are very easily calibrated since they involve a small number of free parameters. As mentioned above, Miller et al. [35] proposed such a modeling, that could generalize the model from Morris et al. [3] in the case of 2-dimensional general flows. The authors note that the same type of model could be applied to 3-dimensional flows, at the cost of higher mathematical complexity though. Here we propose another type of model, similar to the second order fluid modeling, which is well known in polymer rheology [45, 46]. In the context of suspension flows such a model has already been proposed and implemented in computational study [47, 48], although in these papers, stress was chosen to be proportional to $\dot{\gamma}^2$. In the present paper, we are interested in low Reynolds number flows, where the stress scales as $\dot{\gamma}$, so that the model has to be modified. Lhuillier proposed such a model with the relevant scaling in a theoretical paper concerning particle migration [49], which is the starting point of the approach that we follow. Actually, Mahmud et al. [50] explored the same idea in a recent paper, where the authors propose a frame-invariant constitutive relation for the total suspension stress. They determine the free parameters from experimental measurements of viscosity and normal stress differences in shear flow from the literature. We assume here such constitutive relations for the total stress and the particle stress as well, since the latter is also needed for the computation of the particle migration flux. The free parameters are determined from discrete simulation data in shear flow [28, 12, 8].

The paper is organized as follows. Section 2 specifies the mathematical modeling : we first deduce the governing equations of the Suspension Balance Model from the two-fluid balance equations for momentum and mass and the material functions deduced from discrete simulations are shown. The frame-invariant model allowing to compute the total and contact stresses is explained, and the form it takes for various standard homogeneous flows is examined. Also, part of this section is devoted to the expected limitations of the model. The numerical implementation using the finite volume toolbox OpenFOAM is explained in section 3. In section 4, the velocity and volume fraction distributions are computed for various standard flows of interest. The results are compared whenever possible to theoretical predictions or experimental measurements, emphasizing the range of applicability of the approach. Finally, a brief conclusion ends the paper in section 5.

2. Mathematical modeling

2.1. Governing equations

We consider rigid spherical particles of radius a and density ρ_p in suspension within a Newtonian fluid of viscosity η_f and density ρ_f. The suspension is considered as a continuum. Starting from local — at the particle scale — balance equations for mass and momentum, Jackson [29] obtained the macroscopic scale two-phase balance equations by averaging these micro-scale equations over a meso-scale Representative Volume Element containing "many" particles, and that is still significantly smaller than the macroscopic scale. Starting from this two-phase modeling, we shall here proceed with an homogenization process in order to derive a macroscopic scale one-phase modeling. To do this, we will combine the two-phase equations into a single one and then propose closure expressions for some terms to get a one-phase system of equations.

2.1.1. Mass conservation

The volume fraction of the particulate phase in the suspension is noted ϕ. Mass conservation equations for respectively the particulate phase (with subscript p) and the fluid phase (with subscript f) are given by :

$$\frac{\partial \phi \rho_p}{\partial t} + \nabla.(\phi \rho_p \mathbf{v_p}) = 0 \tag{1a}$$

$$\frac{\partial (1-\phi) \rho_f}{\partial t} + \nabla.((1-\phi) \rho_f \mathbf{v_f}) = 0 \tag{1b}$$

where $\mathbf{v_p}$ and $\mathbf{v_f}$ respectively denote the velocity of the particulate and the fluid phases. By summing the two above equations (1), we obtain the mass conservation equation for the mixture :

$$\frac{\partial \rho_m}{\partial t} + \nabla.(\rho_m \mathbf{v_m}) = 0 \tag{2}$$

with ρ_m the mean density of the mixture and $\mathbf{v_m}$ the mass-averaged suspension velocity :

$$\rho_m = \phi \rho_p + (1-\phi) \rho_f \tag{3}$$

$$\mathbf{v_m} = \frac{\phi \rho_p \mathbf{v_p} + (1-\phi) \rho_f \mathbf{v_f}}{\rho_m} \tag{4}$$

Since densities ρ_p and ρ_f are constant, we can also deduce the following equations :

$$\nabla.\mathbf{u} = 0 \tag{5}$$

with $\mathbf{u}$ the volume-averaged suspension velocity :

$$\mathbf{u} = \phi \mathbf{v_p} + (1-\phi) \mathbf{v_f} \tag{6}$$

Eqs. (5) and (6) state that whenever the fluid and particulate phases are both incompressible, the suspension also is. The velocity $\mathbf{v_m}$ is related to the velocity $\mathbf{u}$ by :

$$\mathbf{v_m} = \mathbf{u} + \phi(1-\phi) \frac{\rho_p - \rho_f}{\rho_m} \mathbf{v_{pf}} \tag{7}$$

with $\mathbf{v_{pf}} = \mathbf{v_p} - \mathbf{v_f}$ the relative velocity between the two phases.

2.1.2. Momentum balance

In the two-phase modeling, momentum balance equations for each phases read [30] :

$$\frac{\partial \phi \rho_p \mathbf{v_p}}{\partial t} + \nabla.(\phi \rho_p \mathbf{v_p} \otimes \mathbf{v_p}) = \nabla.\mathbf{\Sigma^c} + \rho_p \phi \mathbf{g} + \mathbf{f} \tag{8a}$$

$$\begin{aligned} \frac{\partial (1-\phi) \rho_f \mathbf{v_f}}{\partial t} + \nabla.((1-\phi) \rho_f \mathbf{v_f} \otimes \mathbf{v_f}) \\ = \nabla.\mathbf{\Sigma^f} + \rho_f (1-\phi) \mathbf{g} - \mathbf{f} \end{aligned} \tag{8b}$$

with $\mathbf{\Sigma^c}$ the particle contact stress tensor and $\mathbf{\Sigma^f}$ the fluid stress tensor (which expression is given in section 2.2) ; $\mathbf{g}$ is gravity and $\mathbf{f}$ denotes the interaction force between the two phases. Deriving a modeled expression for this force is still an open problem [49, 4]. The most commonly used expression for suspensions at low particle-scale Reynolds number writes [51, 30] :

$$\mathbf{f} = \phi \nabla.\mathbf{\Sigma^f} + \alpha(\phi)(\mathbf{v_f} - \mathbf{v_p}) \tag{9}$$

The term $\phi \nabla.\mathbf{\Sigma^f}$ includes buoyancy, $\alpha(\phi)$ is the drag coefficient, which reads, in the case of rigid spheres [5] :

$$\alpha(\phi) = \frac{9\eta_f \phi(1-\phi)^2}{2a^2 f(\phi)} \tag{10}$$

with $f(\phi)$ the empirical hindered settling function. We shall consider here the expression proposed in 1954 by Richardson & Zaki [52], which is given by :

$$f(\phi) = (1-\phi)^{5.1} \tag{11}$$

Summing equations (8) yields the momentum balance equation for the mixture :

$$\begin{aligned} &\frac{\partial \rho_m \mathbf{v_m}}{\partial t} + \nabla.(\phi\rho_p \mathbf{v_p} \otimes \mathbf{v_p} + (1-\phi)\rho_f \mathbf{v_f} \otimes \mathbf{v_f}) \\ &\qquad = \nabla.\mathbf{\Sigma^c} + \nabla.\mathbf{\Sigma^f} + \rho_m \mathbf{g} \end{aligned} \tag{12}$$

The convective flux term of the mixture can be written as :

$$\begin{aligned} &\nabla.(\phi\rho_p \mathbf{v_p} \otimes \mathbf{v_p} + (1-\phi)\rho_f \mathbf{v_f} \otimes \mathbf{v_f}) \\ &= \nabla.(\rho_m \mathbf{v_m} \otimes \mathbf{v_m}) + \nabla.(\frac{\rho_p \rho_f}{\rho_m}\phi(1-\phi)\mathbf{v_{pf}} \otimes \mathbf{v_{pf}}) \end{aligned} \tag{13}$$

The *drift tensor* ($\frac{\rho_p \rho_f}{\rho_m}\phi(1-\phi)\mathbf{v_{pf}} \otimes \mathbf{v_{pf}}$) is denoted by $\tau_\mathbf{D}$ [53]. Eq. (12) then becomes :

$$\begin{aligned} &\frac{\partial \rho_m \mathbf{v_m}}{\partial t} + \nabla.(\rho_m \mathbf{v_m} \otimes \mathbf{v_m}) \\ &\qquad = \nabla.\mathbf{\Sigma^c} + \nabla.\mathbf{\Sigma^f} + \rho_m \mathbf{g} - \nabla.(\tau_\mathbf{D}) \end{aligned} \tag{14}$$

2.1.3. Particulate phase continuity equation

Using equations (1a) and (1b) together with Eq. (9), (8) yields :

$$\begin{aligned} \phi\rho_p \frac{D\mathbf{v_p}}{Dt} &= \nabla.\mathbf{\Sigma^c} + \phi\nabla.\mathbf{\Sigma^f} \\ &\quad + \rho_p \phi \mathbf{g} - \alpha(\phi)\mathbf{v_{pf}} \end{aligned} \tag{15a}$$

$$\begin{aligned} (1-\phi)\rho_f \frac{D\mathbf{v_f}}{Dt} &= (1-\phi)\nabla.\mathbf{\Sigma^f} \\ &\quad + \rho_f (1-\phi)\mathbf{g} + \alpha(\phi)\mathbf{v_{pf}} \end{aligned} \tag{15b}$$

with : $\frac{D\mathbf{v_h}}{Dt} = \frac{\partial \mathbf{v_h}}{\partial t} + (\mathbf{v_h}.\nabla)\mathbf{v_h}$, $h = f$ or p, the material derivative of velocity $\mathbf{v_h}$.

Eliminating $\nabla\cdot\mathbf{\Sigma^f}$, the relative velocity can be written :

$$\begin{aligned} \alpha(\phi)\mathbf{v_{pf}} &= -\phi(1-\phi)\left[\rho_p \frac{D\mathbf{v_p}}{Dt} - \rho_f \frac{D\mathbf{v_f}}{Dt}\right] \\ &\quad + (1-\phi)\nabla.\mathbf{\Sigma^c} + \phi(1-\phi)(\rho_p - \rho_f)\mathbf{g} \end{aligned} \tag{16}$$

2.1.4. Model approximation

Gathering Eq. (1a), (2) and (14) yields the following system of balance equations :

$$\frac{\partial \rho_m}{\partial t} + \nabla.(\rho_m \mathbf{v_m}) = 0 \tag{17a}$$

$$\begin{aligned} &\frac{\partial \rho_m \mathbf{v_m}}{\partial t} + \nabla.(\rho_m \mathbf{v_m} \otimes \mathbf{v_m}) \\ &\qquad = \nabla.\mathbf{\Sigma^c} + \nabla.\mathbf{\Sigma^f} + \rho_m \mathbf{g} - \nabla.(\tau_\mathbf{D}) \end{aligned} \tag{17b}$$

$$\frac{\partial \phi}{\partial t} + \nabla.(\phi \mathbf{v_m}) = -\nabla.(\frac{\rho_f}{\rho_m}\phi(1-\phi)\mathbf{v_{pf}}) \tag{17c}$$

with $\mathbf{v_{pf}}$ given by Eq. (16). Eq. (1a) has been modified using (4) to get Eq. (17c). This system, which was used in [53, 54] is named *mixture model*. However, this model is still a two-phase model since it needs two velocity fields. In order to remove one phase in the modeling and build a one-phase modeling, we propose an approximation that consists in assuming that the relative velocity is negligible with respect to the average velocity, in all the inertial terms. This assumption implies that the term $\nabla.(\tau_\mathbf{D})$ vanishes and :

$$\frac{D\mathbf{v_p}}{Dt} \approx \frac{D\mathbf{v_f}}{Dt} \approx \frac{D\mathbf{v_m}}{Dt} \approx \frac{D\mathbf{u}}{Dt} \tag{18}$$

This approximation will actually be fulfilled for every numerical test we have run. The expression for the relative velocity (16) can hence be simplified as :

$$\frac{\alpha(\phi)}{1-\phi}\mathbf{v_{pf}} = \nabla.\mathbf{\Sigma^c} + \phi(\rho_p - \rho_f)\left[\mathbf{g} - \frac{D\mathbf{u}}{Dt}\right] \tag{19}$$

and the momentum equation (17b) becomes :

$$\frac{\partial \rho_m \mathbf{u}}{\partial t} + \nabla.(\rho_m \mathbf{u} \otimes \mathbf{u}) = \nabla.(\mathbf{\Sigma^c} + \mathbf{\Sigma^f}) + \rho_m \mathbf{g} \tag{20}$$

Rewriting Eq. (17a) and (17c) as a function of $\mathbf{u}$, the volume-averaged suspension velocity, we now obtain the following system of governing equations :

$$\nabla.\mathbf{u} = 0 \tag{21a}$$

$$\frac{\partial \rho_m \mathbf{u}}{\partial t} + \nabla.(\rho_m \mathbf{u} \otimes \mathbf{u}) = \nabla.(\mathbf{\Sigma^c} + \mathbf{\Sigma^f}) + \rho_m \mathbf{g} \tag{21b}$$

$$\frac{\partial \phi}{\partial t} + \nabla.(\phi \mathbf{u}) = -\nabla.(\phi(1-\phi)\mathbf{v_{pf}}) \tag{21c}$$

$$\phi(1-\phi)\mathbf{v_{pf}} = \frac{2a^2 f(\phi)}{9\eta_f} \times \left(\phi(\rho_p - \rho_f)\left[\mathbf{g} - \frac{D\mathbf{u}}{Dt}\right] + \nabla.\mathbf{\Sigma^c}\right) \tag{21d}$$

Equations (21c) and (21d) govern the transport of particles by convection, according to the velocity field $\mathbf{u}$. Migration is governed by the divergence of the contact stress tensor. The gravity term, corrected by the suspension acceleration, describes the particles sedimentation. Note that Eq. (21d) defines the RHS of the solid volume fraction transport equation (21c). The velocity field $\mathbf{u}$ is given by the equations (21a) and (21b) and the coupling will be done by ρ_m, $\mathbf{\Sigma^c}$ and $\mathbf{\Sigma^f}$. We will now close the system by giving the constitutive equations for the stresses.

2.2. Constitutive equations

2.2.1. Material functions in simple shear flow

According to [49, 4], the total stress of the suspension mixture, sum of the fluid and contact contributions $\mathbf{\Sigma} = \mathbf{\Sigma^f} + \mathbf{\Sigma^c}$ can be expressed as :

$$\mathbf{\Sigma} = -(1-\phi)p^f \mathbf{I} + 2\eta_f \mathbf{E} + \mathbf{\Sigma^{pf}} + \mathbf{\Sigma^c} \tag{22}$$

with p^f the average fluid pressure, $\mathbf{E}$ the average deformation rate tensor of the suspension, $\mathbf{I}$ the identity tensor ; $\mathbf{\Sigma^{pf}}$ denotes the hydrodynamic contribution from fluid-particle interactions while $\mathbf{\Sigma^c}$ refers to the particle-particle contact contribution. The fluid stress tensor can then be defined as follows :

$$\mathbf{\Sigma^f} = -(1-\phi)p^f \mathbf{I} + 2\eta_f \mathbf{E} + \mathbf{\Sigma^{pf}} \tag{23}$$

Most of experiments and numerical calculations currently available in the literature deal with simple shear flow, where the stresses $\mathbf{\Sigma}$ and $\mathbf{\Sigma^c}$ are expressed in terms of parameters called material functions. In the present study, these have been determined using discrete simulations [28, 8, 12] and are given below. Simple shear flow is defined as (see figure 1) :

$$\mathbf{u} = 2ey\mathbf{e_x},\ \mathbf{E} = \begin{pmatrix} 0 & e & 0 \\ e & 0 & 0 \\ 0 & 0 & 0 \end{pmatrix} \text{ and } \dot{\gamma} = 2|e|$$

The tangential stress depends on volume fraction ϕ and, at first order, is a linear function of $\dot{\gamma}$. In addition, anisotropic normal stresses are also function of ϕ and proportional to $\dot{\gamma}$. However, for the total stress, we are only interested in the normal stress differences which are defined as $N_1 = \Sigma_{11} - \Sigma_{22}$ and $N_2 = \Sigma_{22} - \Sigma_{33}$. Indeed, since we deal with incompressible flows, the spherical part of the stress tensor corresponds to pressure. Even if additional terms are present in the modeling, the pressure will always adapt to ensure that the flow remains incompressible. The total stress can be expressed as :

$$\mathbf{\Sigma} = -p\mathbf{I} + dev(\mathbf{\Sigma}) \tag{24}$$

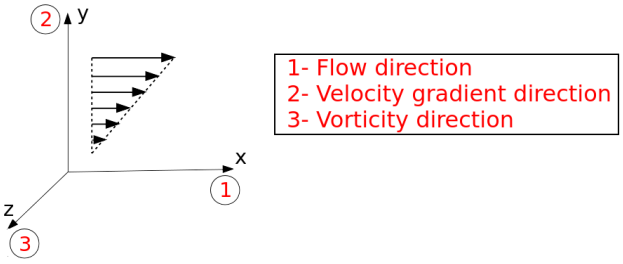

FIGURE 1: Flow direction in a simple shear

The material functions for the total stress deviator, obtained from a best fit of simulation data [28, 8, 12], are :

$$dev(\mathbf{\Sigma}) = 2\eta_f\eta_s(\phi)\mathbf{E} + \eta_f\eta_s(\phi)\dot{\gamma}\times \begin{pmatrix} \frac{1}{3}(2\hat{N}_1+\hat{N}_2) & 0 & 0 \\ 0 & \frac{1}{3}(-\hat{N}_1+\hat{N}_2) & 0 \\ 0 & 0 & \frac{1}{3}(-\hat{N}_1-2\hat{N}_2) \end{pmatrix} \quad (25)$$

- Effective viscosity :

$$\eta_s = \left(1 + \frac{\frac{5}{4}\phi}{1-\frac{\phi}{\phi_m}}\right)^2 \quad (26)$$

- Jamming concentration :

$$\phi_m = 0.583 \quad (27)$$

- Normal stress differences :

$$\hat{N}_1 = \frac{N_1}{\eta_f\eta_s\dot{\gamma}} = a_1\left(\frac{\phi}{\phi_m}\right)^2 + a_2\left(\frac{\phi}{\phi_m}\right)^4 + a_3\left(\frac{\phi}{\phi_m}\right)^6 \quad (28a)$$

$$\hat{N}_1 + 2\hat{N}_2 = \frac{N_1+2N_2}{\eta_f\eta_s\dot{\gamma}} = b_1\left(\frac{\phi}{\phi_m}\right)^2 + b_2\left(\frac{\phi}{\phi_m}\right)^4 + b_3\left(\frac{\phi}{\phi_m}\right)^6 \quad (28b)$$

With :

$$a_1 = -0.1352\ a_2 = -0.3174\ a_3 = 0.4656$$
$$b_1 = -0.3551\ b_2 = -3.4660\ b_3 = 3.2913$$

The contact stress $\mathbf{\Sigma^c}$ can be completely determined from the simulations, including the isotropic part :

$$\mathbf{\Sigma^c} = 2\eta_c\eta_f\mathbf{E} + \eta_f\eta_s(\phi)\dot{\gamma}\begin{pmatrix} \hat{\Sigma}^c_{11}(\frac{\phi}{\phi_m}) & 0 & 0 \\ 0 & \hat{\Sigma}^c_{22}(\frac{\phi}{\phi_m}) & 0 \\ 0 & 0 & \hat{\Sigma}^c_{33}(\frac{\phi}{\phi_m}) \end{pmatrix} \quad (29)$$

- Contact viscosity :

$$\frac{\eta_c}{\eta_s} = c_1\left(\frac{\phi}{\phi_m}\right)^4 + c_2\left(\frac{\phi}{\phi_m}\right)^5 \quad (30)$$

with $c_1 = 4.4659$ and $c_2 = 1 - c_1$

- Contact stress :

$$\hat{\Sigma}^c_{11} = \frac{\Sigma^c_{11}}{\eta_f\eta_s\dot{\gamma}} = d_1\left(\frac{\phi}{\phi_m}\right)^{d_2} \quad (31a)$$

$$\hat{\Sigma}^c_{22} = \frac{\Sigma^c_{22}}{\eta_f\eta_s\dot{\gamma}} = \hat{\Sigma}^c_{11}\left(e_1 + e_2\frac{\phi}{\phi_m} + e_3\left(\frac{\phi}{\phi_m}\right)^2\right) \quad (31b)$$

$$\hat{\Sigma}^c_{33} = \frac{\Sigma^c_{33}}{\eta_f\eta_s\dot{\gamma}} = \hat{\Sigma}^c_{11}\left(f_1 + f_2\frac{\phi}{\phi_m} + f_3\left(\frac{\phi}{\phi_m}\right)^4\right) \quad (31c)$$

with

$$d_1 = -2.4247\ d_2 = 4.128$$
$$e_1 = 2.1446\ e_2 = -2.7234\ e_3 = 1.5759$$
$$f_1 = 0.3750\ f_2 = 0.0366\ f_3 = 0.4846$$

All material functions are displayed in the Appendix. Part of the simulation data that the functions are fitted to, namely η^S, N_1, N_2 and Σ^c_{22}, have been shown to compare reasonably well with experimental and simulation data from the literature [5].

2.2.2. Frame-invariant modeling

The expressions of both tensors $\mathbf{\Sigma}$ and $\mathbf{\Sigma^c}$ (Eq. (25) and Eq. (29)) are obtained from the situation of a simple shear flow. Strictly speaking, they should hence be valid only for this particular type of flow and thus are not adapted to general flow situations. We shall therefore try and generalize this modeling to general flows and geometries. To this purpose, a frame-invariant modeling is proposed in the following.

General formulation of the stress.

Lhuillier [49], following the work by Rivlin and Ericksen [55], proposes a frame-invariant expression for the stress, that takes into account the experimentally measured quantities and, in particular, the normal stress differences. The proposed modeling in [49] reads as

$$\mathbf{\Sigma} = \beta_0 \mathbf{I} + 2\beta_1 \mathbf{E} + 4\beta_2 \mathbf{E}.\mathbf{E} + \beta_3 \frac{\mathcal{D}\mathbf{E}}{\mathcal{D}t} \tag{32}$$

with β_i is a function of $\dot{\gamma}$ and ϕ; $\frac{\mathcal{D}\mathbf{E}}{\mathcal{D}t}$ denotes the Jaumann derivative of the tensor $\mathbf{E}$, and is defined as :

$$\frac{\mathcal{D}\mathbf{E}}{\mathcal{D}t} = \frac{\partial \mathbf{E}}{\partial t} + (\mathbf{u}.\nabla)\mathbf{E} + \mathbf{E}.\mathbf{\Omega} - \mathbf{\Omega}.\mathbf{E} \tag{33}$$

The tensors $\mathbf{E}$ and $\mathbf{\Omega}$ are respectively the deformation rate and vorticity tensors, defined in index notation as $E_{ij} = 1/2\ (\partial u_i/\partial x_j + \partial u_j/\partial x_i)$, $\Omega_{ij} = 1/2\ (\partial u_i/\partial x_j - \partial u_j/\partial x_i)$. The shear rate is also defined as $\dot{\gamma} = \sqrt{2\mathbf{E} : \mathbf{E}}$.

Eq. (32) is commonly used in the context of polymer rheology. This model, which is considered in that field as a simplified model for slowly varying visco-elastic fluids in slow motion [45, 56], defines the so-called second-order fluid. It has also been used in the modeling of granular flows [57] as well as in the field of suspensions rheology [47, 48, 58], with quite different material functions though. In low Reynolds number suspension flows, the fluid mixture is not visco-elastic, the stresses depend on the volume fraction ϕ and can be, at first order in a simple shear flow, be considered as a linear function of $\eta_f \dot{\gamma}$ [5]. Indeed, the purpose here is not to describe rate-dependent behaviour such as discontinuous shear-thickening [27], or shear-thinning [8]. At the same order of approximation, and also considering the absence of inertia at the particle scale ($Re_p = \frac{\rho_f a^2 \dot{\gamma}}{\eta_f} \ll 1$) and the high stiffness of the contact force between particles [12], the only relevant characteristic time in the problem is given by the shear rate. As a consequence, the relevant dynamic parameter is deformation, and not time [6, 11, 12]. Eq. (32) is modified accordingly.

$$\mathbf{\Sigma} = \eta_f \dot{\gamma} \left[\psi_0(\phi)\mathbf{I} + 2\psi_1(\phi)\ \hat{\mathbf{E}} + 4\psi_2(\phi)\hat{\mathbf{E}}.\hat{\mathbf{E}} + \psi_3(\phi)\frac{1}{\dot{\gamma}}\frac{\mathcal{D}\hat{\mathbf{E}}}{\mathcal{D}t} \right] \tag{34}$$

where the reduced strain rate is defined as $\hat{\mathbf{E}} = \mathbf{E}/\dot{\gamma}$.

Eq. (34) therefore provides a general expression for the stress tensor, that remains invariant under any time-dependant combination of rotation and translation [55, 59]. The reduced strain rate $\hat{\mathbf{E}}$ defines the type of extensional straining motion undergone by the fluid (planar, uniaxial, biaxial etc.) independently of its intensity which is measured by the strain rate $\dot{\gamma}$. In the present modeling of a rate independent suspension, the stresses are proportional to the strain rate. The terms inside the round brackets are supposed to define the influence of the local flow geometry and history on the underlying shear-induced microstructure. We note that Lhuillier [49] proposed a slightly different expression for the last term inside the round brackets, namely $\frac{1}{\dot{\gamma}^2}\frac{\mathcal{D}\mathbf{E}}{\mathcal{D}t}$. As explained in section 2.2.5, Eq. (34) fits closer to the experimental measurements performed in time varying simple shear flow.

As recalled previously, the Jaumann derivative $\frac{\mathcal{D}}{\mathcal{D}t}$ has been extensively used in the modeling of polymer rheology. The Jaumann derivative of a tensor field is the material derivative of this quantity as seen by an observer attached to the fluid and that rotates at the angular velocity $\mathbf{\Omega}$ of the fluid [45]. The idea is that, as the moving and rotating fluid "sees" a varying reduced strain rate tensor, the microstructure is affected, and so is the stress. Due to the prefactor $1/\dot{\gamma}$, this derivative should be understood as a variation per unit strain. The corresponding term — the last term of the RHS in Eq. (34) — which, as shown below, is instrumental for accounting for the first normal stress difference in simple shear flow, may be conveniently expressed in a slightly different way.

The material derivative of the reduced strain rate tensor can be split in two contributions. The derivation can be easily carried out in the eigenframe, i.e. the frame of the eigenvectors $\{\mathbf{e_i}\}$ of the strain rate tensor attached to the suspension. The reduced deformation rate tensor is written using the reduced principal rates of strain $\hat{\xi}_i = \xi_i/\dot{\gamma}$:

$$\hat{\mathbf{E}} = \sum_{i=1}^{3} \hat{\xi}_i \ \mathbf{e_i} \otimes \mathbf{e_i} \tag{35}$$

So that the material derivative reads [45] :

$$\frac{D\hat{\mathbf{E}}}{Dt} = \sum_{i=1}^{3} \frac{D\hat{\xi}_i}{Dt} \mathbf{e_i} \otimes \mathbf{e_i} + \mathbf{\Omega}_F.\hat{\mathbf{E}} - \hat{\mathbf{E}}.\mathbf{\Omega}_F \tag{36}$$

where $\mathbf{\Omega}_F$ is the angular velocity tensor of the frame $\{\mathbf{e_i}\}$. From Eqs. (33) and (36), the Jaumann derivative of the strain rate tensor reads :

$$\frac{\mathcal{D}\hat{\mathbf{E}}}{\mathcal{D}t} = \sum_{i=1}^{3} \frac{D\hat{\xi}_i}{Dt} \mathbf{e_i} \otimes \mathbf{e_i} + \mathbf{\Delta\Omega}.\hat{\mathbf{E}} - \hat{\mathbf{E}}.\mathbf{\Delta\Omega} \tag{37}$$

where the angular velocity tensor of the eigenframe $\{\mathbf{e_i}\}$ with respect to the rotating fluid is given by :

$$\mathbf{\Delta\Omega} = \mathbf{\Omega}_F - \mathbf{\Omega}. \tag{38}$$

The first term of the RHS of Eq.(37), which is connected to the variation of the principal rates of the reduced strain rate tensor, is the material derivative of $\hat{\mathbf{E}}$ in the frame $\{\mathbf{e_i}\}$, while the second term originates in the rotation of this frame with respect to the rotating fluid [45, 60]. The relative angular velocity tensor $\mathbf{\Delta\Omega}$ has been introduced in particular in the context of polymers [61] and suspensions [35] rheology modeling. Eqs. (37) and (38) allow categorization of the flows that will be considered in the following sections (see also ref. [61]).

The free material function $\psi_i(\phi)$ for the total stress and the contact stress will now be stated. It should be noted here that Mahmud et al. [50] (see also [62]) proposed recently a frame-invariant constitutive relation very close to the expression from (34) to compute the total stress. In this paper, the author deduced the free material functions they needed from experimental measurements. Since we need the constitutive relations for the contact stress as well, we decided to determine the complete set of material functions from the discrete numerical simulation data presented in section 2.2.1.

Determination of the coefficients ψ_i for the total stress. Let us now express the coefficients ψ_i in Eq. (34) as a function of our material functions, defined by Eq. (25)—(31).

As mentioned above, the incompressibility of the flow allows us to only focus on the deviatoric part, instead of the entire total stress tensor :

$$\mathbf{\Sigma} = -p\mathbf{I} + dev(\mathbf{\Sigma}) \tag{39}$$

The deviator stress tensor $dev(\mathbf{\Sigma})$ is given by :

$$\begin{aligned} dev(\mathbf{\Sigma}) = \eta_f \dot{\gamma} \Big[& 2\psi_1(\phi)\hat{\mathbf{E}} \\ & + 4\psi_2(\phi) \left(\hat{\mathbf{E}}.\hat{\mathbf{E}} - \frac{tr(\hat{\mathbf{E}}.\hat{\mathbf{E}})}{3} I \right) \\ & + \psi_3(\phi) \frac{1}{\dot{\gamma}} \frac{\mathcal{D}\hat{\mathbf{E}}}{\mathcal{D}t} \Big] \end{aligned} \tag{40}$$

If we consider the case of a simple shear $\mathbf{u} = 2\,e\,y\,\mathbf{e_x}$, the tensors $\mathbf{E}$ and $\mathbf{\Omega}$ read :

$$\mathbf{E} = \begin{pmatrix} 0 & e & 0 \\ e & 0 & 0 \\ 0 & 0 & 0 \end{pmatrix} \quad \mathbf{\Omega} = \begin{pmatrix} 0 & e & 0 \\ -e & 0 & 0 \\ 0 & 0 & 0 \end{pmatrix} \tag{41}$$

with, in this case, $\dot{\gamma} = 2|e|$. In addition, the strain rate tensor is stationary in the frame at rest, so that $\mathbf{\Omega}_F = 0$ and $\frac{D\hat{\xi}_i}{Dt} = 0$. In that case the Jaumann derivative accounts for the rotation $-\mathbf{\Omega}$ of the reduced strain rate tensor with respect to the fluid. In particular :

$$\frac{\mathcal{D}\hat{\mathbf{E}}}{\mathcal{D}t} = -\mathbf{\Omega}.\hat{\mathbf{E}} + \hat{\mathbf{E}}.\mathbf{\Omega} = \frac{\dot{\gamma}}{2} \begin{pmatrix} -1 & 0 & 0 \\ 0 & 1 & 0 \\ 0 & 0 & 0 \end{pmatrix} \tag{42}$$

The expression for the deviator (see Eq. (40)) hence becomes :

$$dev(\mathbf{\Sigma}) = \eta_f \dot{\gamma} \left[\text{sign}(e)\psi_1(\phi) \begin{pmatrix} 0 & 1 & 0 \\ 1 & 0 & 0 \\ 0 & 0 & 0 \end{pmatrix} + \psi_2(\phi) \begin{pmatrix} \frac{1}{3} & 0 & 0 \\ 0 & \frac{1}{3} & 0 \\ 0 & 0 & -\frac{2}{3} \end{pmatrix} + \psi_3(\phi) \begin{pmatrix} -\frac{1}{2} & 0 & 0 \\ 0 & \frac{1}{2} & 0 \\ 0 & 0 & 0 \end{pmatrix} \right] \tag{43}$$

where sign(e) denotes the sign of e. When identifying the terms of the above equation (43) with those of Eq. (25), one can deduce the expressions of the ψ_i coefficients :

$$\begin{aligned} \psi_1 &= \eta_s \\ \psi_2 &= \frac{N_1 + 2N_2}{2\eta_f \dot{\gamma}} = \eta_s \frac{(\hat{N}_1 + 2\hat{N}_2)}{2} \\ \psi_3 &= -\frac{N_1}{\eta_f \dot{\gamma}} = -\eta_s \hat{N}_1 \end{aligned} \tag{44}$$

Note that if the flow changes direction, then the term in ψ_1 (shear stress) changes sign while the other terms (normal stresses) do not, as expected from symmetry argument.

Determination of the coefficients ψ_i^c for the contact stress. The same approach was used for the contact stress tensor to derive its frame-invariant form :

$$\mathbf{\Sigma^c} = \eta_f \dot{\gamma} \left(\psi_0^c(\phi)\mathbf{I} + 2\psi_1^c(\phi)\hat{\mathbf{E}} + 4\psi_2^c(\phi)\hat{\mathbf{E}}.\hat{\mathbf{E}} + \psi_3^c(\phi)\frac{1}{\dot{\gamma}}\frac{\mathcal{D}\hat{\mathbf{E}}}{\mathcal{D}t} \right) \tag{45}$$

We consider the case of a simple shear flow :

$$\mathbf{\Sigma^c} = \eta_f \dot{\gamma} \left[\psi_0^c(\phi) \begin{pmatrix} 1 & 0 & 0 \\ 0 & 1 & 0 \\ 0 & 0 & 1 \end{pmatrix} + sign(e)\psi_1^c(\phi) \begin{pmatrix} 0 & 1 & 0 \\ 1 & 0 & 0 \\ 0 & 0 & 0 \end{pmatrix} + \psi_2^c(\phi) \begin{pmatrix} 1 & 0 & 0 \\ 0 & 1 & 0 \\ 0 & 0 & 0 \end{pmatrix} + \psi_3^c(\phi) \begin{pmatrix} -\frac{1}{2} & 0 & 0 \\ 0 & \frac{1}{2} & 0 \\ 0 & 0 & 0 \end{pmatrix} \right] \tag{46}$$

Again, identifying this expression with Eq. (29) yields :

$$\begin{aligned} \psi_0^c &= \eta_s \hat{\Sigma}_{33}^c \\ \psi_1^c &= \eta_c \\ \psi_2^c &= \eta_s \left(\frac{\hat{\Sigma}_{11}^c + \hat{\Sigma}_{22}^c}{2} - \hat{\Sigma}_{33}^c \right) \\ \psi_3^c &= -\eta_s (\hat{\Sigma}_{11}^c - \hat{\Sigma}_{22}^c) \end{aligned} \tag{47}$$

Note that in this case, all terms in the tensor $\mathbf{\Sigma^c}$, including the isotropic part, must be determined.

2.2.3. Application to rheometrical flows

In this section, we apply the present frame-invariant modeling to two classical rheological flows widely analyzed in the experimental context, namely steady Couette flow and torsional parallel plate flow. In their paper concerning shear-induced migration in curvilinear flow, Morris and Boulay [3] approximated such flows by simple shear flows. We recall below that they are not strictly speaking simple shear flows. However, the present model yields the same formal expression for the stresses as in Eq. (43) and (46), which hold for simple shear flows.

• For the cylindrical Couette flow, the velocity field is of the form $\mathbf{u} = u_\theta(r)\mathbf{e}_\theta$, the gradient of which is :

$$\nabla \otimes \mathbf{u} = \begin{pmatrix} 0 & -\frac{u_\theta}{r} & 0 \\ \frac{du_\theta}{dr} & 0 & 0 \\ 0 & 0 & 0 \end{pmatrix} \tag{48}$$

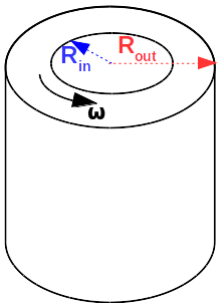

FIGURE 2: Couette flow geometry.

The corresponding strain rate and vorticity tensors and read :

$$\begin{aligned}\mathbf{E} =& \frac{1}{2}\left(\frac{du_\theta}{dr} - \frac{u_\theta}{r}\right)\begin{pmatrix}0 & 1 & 0\\ 1 & 0 & 0\\ 0 & 0 & 0\end{pmatrix}\\ \mathbf{\Omega} =& -\frac{1}{2}\left(\frac{du_\theta}{dr} + \frac{u_\theta}{r}\right)\begin{pmatrix}0 & 1 & 0\\ -1 & 0 & 0\\ 0 & 0 & 0\end{pmatrix}\end{aligned} \tag{49}$$

with the shear rate defined as $\dot{\gamma} = |\frac{du_\theta}{dr} - \frac{u_\theta}{r}|$. The angular velocity of the frame moving and rotating with the fluid is given by :

$$\mathbf{\Omega}_F = \begin{pmatrix}0 & -\frac{u_\theta}{r} & 0\\ \frac{u_\theta}{r} & 0 & 0\\ 0 & 0 & 0\end{pmatrix} \tag{50}$$

The Jaumann derivative is completely specified by relative angular velocity :

$$\begin{aligned}\mathbf{\Delta\Omega} &= \mathbf{\Omega}_F - \mathbf{\Omega}\\ &= -\frac{1}{2}\left(\frac{du_\theta}{dr} - \frac{u_\theta}{r}\right)\begin{pmatrix}0 & -1 & 0\\ 1 & 0 & 0\\ 0 & 0 & 0\end{pmatrix}\end{aligned} \tag{51}$$

yielding :

$$\frac{\mathcal{D}\hat{\mathbf{E}}}{\mathcal{D}t} = \mathbf{\Delta\Omega}.\hat{\mathbf{E}} - \hat{\mathbf{E}}.\mathbf{\Delta\Omega} = \frac{\dot{\gamma}}{2}\begin{pmatrix}1 & 0 & 0\\ 0 & -1 & 0\\ 0 & 0 & 0\end{pmatrix} \tag{52}$$

The contact stress tensor then writes :

$$\begin{aligned}\mathbf{\Sigma^c} =& 2\eta_f\eta_c\mathbf{E}\\ &+ \eta_f\eta_s\dot{\gamma}\left[\hat{\Sigma}^c_{33}\mathbf{I} + \left(\frac{\hat{\Sigma}^c_{11}+\hat{\Sigma}^c_{22}}{2} - \hat{\Sigma}^c_{33}\right)\begin{pmatrix}1 & 0 & 0\\ 0 & 1 & 0\\ 0 & 0 & 0\end{pmatrix}\right.\\ &\left. - \frac{\hat{\Sigma}^c_{22}-\hat{\Sigma}^c_{11}}{2}\begin{pmatrix}-1 & 0 & 0\\ 0 & 1 & 0\\ 0 & 0 & 0\end{pmatrix}\right]\end{aligned} \tag{53}$$

yielding :

$$\mathbf{\Sigma^c} = 2\eta_f\eta_c\mathbf{E} + \eta_f\eta_s\dot{\gamma}\begin{pmatrix}\hat{\Sigma}^c_{22} & 0 & 0\\ 0 & \hat{\Sigma}^c_{11} & 0\\ 0 & 0 & \hat{\Sigma}^c_{33}\end{pmatrix} \tag{54}$$

While this flow is not a simple shear flow since $||\mathbf{E}|| \neq ||\mathbf{\Omega}||$, we observe that the contact stress is equivalent to the one that would be found in simple shear flow using Eq. (29) with the shear rate $\dot{\gamma}$ and, according to figure 1, $e_r = e_2$, $e_\theta = e_1$ and $e_z = -e_3$. This is easily understood, inspecting the only contribution that could differ, i.e. the Jaumann derivative. In both cases, the derivative originates in the relative rotation, that amounts to $-\mathbf{\Omega}$ in the simple shear flow (Eq. (42)) and to $\mathbf{\Delta\Omega}$ in the cylindrical Couette flow (Eq. (52)). Since $\mathbf{E}$ and $-\mathbf{\Delta\Omega}$ define together a simple shear flow, as shown by Eqs. (49) and (51), it follows that the expression of the Jaumann derivative is the same as in the case of a simple shear flow. The same conclusion holds for the total stress. As a consequence, the present frame-invariant model for the stresses does not introduce any difference between a cylindrical Couette flow and a simple shear flow.

- For the torsional parallel plate flow, the velocity is of the form $\mathbf{u} = u_\theta(r,z)\mathbf{e}_\theta$, with $u_\theta = \frac{\omega r z}{h}$. The velocity gradient reads :

$$\nabla \otimes \mathbf{u} = \begin{pmatrix} 0 & -\frac{\omega z}{h} & 0 \\ \frac{\omega z}{h} & 0 & \frac{\omega r}{h} \\ 0 & 0 & 0 \end{pmatrix} \tag{55}$$

with the shear rate and angular velocity tensors :

$$\begin{aligned} \mathbf{E} &= \frac{1}{2}\frac{\omega r}{h}\begin{pmatrix} 0 & 0 & 0 \\ 0 & 0 & 1 \\ 0 & 1 & 0 \end{pmatrix} \\ \mathbf{\Omega} &= \frac{1}{2}\begin{pmatrix} 0 & -2\frac{\omega z}{h} & 0 \\ 2\frac{\omega z}{h} & 0 & \frac{\omega r}{h} \\ 0 & -\frac{\omega r}{h} & 0 \end{pmatrix} \end{aligned} \tag{56}$$

and the shear rate :$\dot{\gamma} = |\frac{\omega r}{h}|$

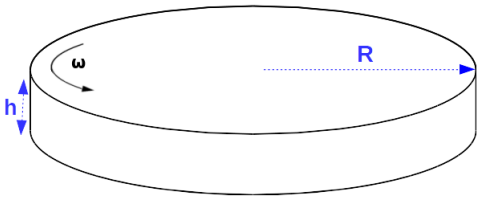

FIGURE 3: Torsional flow geometry.

The angular velocity of the frame moving and rotating with the fluid is given by :

$$\mathbf{\Omega}_F = \begin{pmatrix} 0 & -\frac{\omega z}{h} & 0 \\ \frac{\omega z}{h} & 0 & 0 \\ 0 & 0 & 0 \end{pmatrix} \tag{57}$$

Again, the Jaumann derivative is completely specified by relative angular velocity :

$$\mathbf{\Delta\Omega} = \mathbf{\Omega}_F - \mathbf{\Omega} = \frac{1}{2}\frac{\omega r}{h}\begin{pmatrix} 0 & 0 & 0 \\ 0 & 0 & -1 \\ 0 & 1 & 0 \end{pmatrix} \tag{58}$$

yielding :

$$\frac{\mathcal{D}\hat{\mathbf{E}}}{\mathcal{D}t} = \mathbf{\Delta\Omega}.\hat{\mathbf{E}} - \hat{\mathbf{E}}.\mathbf{\Delta\Omega} = \frac{\dot{\gamma}}{2}\begin{pmatrix} 0 & 0 & 0 \\ 0 & -1 & 0 \\ 0 & 0 & 1 \end{pmatrix} \tag{59}$$

The contact stress tensor for torsional flow is finally given by :

$$\mathbf{\Sigma^c} = 2\eta_f\eta_c\mathbf{E} + \eta_f\eta_s\dot{\gamma}\begin{pmatrix} \hat{\Sigma}^c_{33} & 0 & 0 \\ 0 & \hat{\Sigma}^c_{11} & 0 \\ 0 & 0 & \hat{\Sigma}^c_{22} \end{pmatrix} \tag{60}$$

Again, the expression of the contact stress in a simple shear flow is recovered assuming $e_r = e_3$, $e_\theta = e_1$ and $e_z = e_2$, for the same reason as in cylindrical Couette flow. This results holds for the total stress too.

2.2.4. Application to extensional flows

In this section, we show how the model that we propose deals with homogeneous steady extensional flows (EF). The main trends are then discussed against available simulations and experimental studies from the literature. We shall successively address the planar, uniaxial and the biaxial EF. For all three cases, the strain rate is constant and uniform, and no rotation occurs so that $\frac{\mathcal{D}\hat{\mathbf{E}}}{\mathcal{D}t} = 0$.

- **Planar extension** :

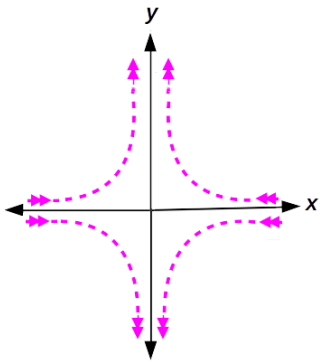

FIGURE 4: Planar extensional flow

Starting with the planar extension, the deformation rate tensor is here defined as :

$$\mathbf{E} = \begin{pmatrix} -\dot{\epsilon} & 0 & 0 \\ 0 & \dot{\epsilon} & 0 \\ 0 & 0 & 0 \end{pmatrix} \tag{61}$$

with $\dot{\epsilon}$ the extension rate. Then, $\dot{\gamma} = ||\mathbf{E}|| = \sqrt{2\mathbf{E} : \mathbf{E}} = 2\dot{\epsilon}$ and $\hat{\mathbf{E}}$ reads :

$$\hat{\mathbf{E}} = \frac{\mathbf{E}}{\dot{\gamma}} = \begin{pmatrix} -\frac{1}{2} & 0 & 0 \\ 0 & \frac{1}{2} & 0 \\ 0 & 0 & 0 \end{pmatrix} \tag{62}$$

and the total stress from Eqs.(39) and (40) writes :

$$\begin{aligned} \mathbf{\Sigma} &= -p\mathbf{I} + 2\eta_f\eta_s\dot{\gamma}\hat{\mathbf{E}} \\ &+ 2\eta_f\eta_s\dot{\gamma}(\hat{N}_1 + 2\hat{N}_2)\left(\hat{\mathbf{E}}.\hat{\mathbf{E}} - \frac{tr(\hat{\mathbf{E}}.\hat{\mathbf{E}})}{3}I\right) \end{aligned} \tag{63}$$

or, in a more explicit form :

$$\begin{aligned} \mathbf{\Sigma} &= -p\mathbf{I} \\ &+ \eta_f\eta_s\dot{\gamma}\begin{pmatrix} -1 + \frac{\hat{N}_1+2\hat{N}_2}{6} & 0 & 0 \\ 0 & 1 + \frac{\hat{N}_1+2\hat{N}_2}{6} & 0 \\ 0 & 0 & -\frac{\hat{N}_1+2\hat{N}_2}{3} \end{pmatrix} \end{aligned} \tag{64}$$

The extensional viscosity η_E can then be computed, as :

$$\eta_E = \frac{\Sigma_{22} - \Sigma_{11}}{\dot{\epsilon}} = 2\frac{\Sigma_{22} - \Sigma_{11}}{\dot{\gamma}} = 4\eta_f\eta_s \tag{65}$$

- **Uniaxial extension** :

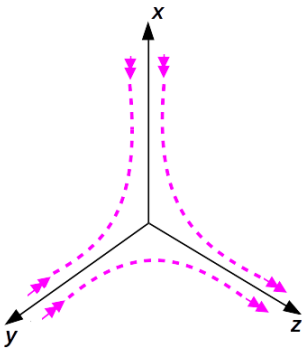

FIGURE 5: Uniaxial extensional flow

Here, the deformation rate tensor writes :

$$\mathbf{E} = \begin{pmatrix} -\frac{\dot{\epsilon}}{2} & 0 & 0 \\ 0 & -\frac{\dot{\epsilon}}{2} & 0 \\ 0 & 0 & \dot{\epsilon} \end{pmatrix} \tag{66}$$

and $\dot{\gamma} = ||\mathbf{E}|| = \sqrt{2\mathbf{E} : \mathbf{E}} = \sqrt{3}\dot{\epsilon}$ so that :

$$\hat{\mathbf{E}} = \frac{\mathbf{E}}{\dot{\gamma}} = \begin{pmatrix} -\frac{1}{2\sqrt{3}} & 0 & 0 \\ 0 & -\frac{1}{2\sqrt{3}} & 0 \\ 0 & 0 & \frac{1}{\sqrt{3}} \end{pmatrix} \tag{67}$$

The total stress (39) can be expressed as :

$$\begin{aligned} \mathbf{\Sigma} &= -p\mathbf{I} \\ &+ \eta_f\eta_s\dot{\gamma}\left(\frac{2}{\sqrt{3}} + \frac{\hat{N}_1 + 2\hat{N}_2}{3}\right)\begin{pmatrix} -\frac{1}{2} & 0 & 0 \\ 0 & -\frac{1}{2} & 0 \\ 0 & 0 & 1 \end{pmatrix} \end{aligned} \tag{68}$$

This enables us to compute the extensional viscosity :

$$\begin{aligned} \eta_E &= \frac{\Sigma_{33} - \Sigma_{11}}{\dot{\epsilon}} \\ &= 3\eta_f\eta_s(1 + \frac{\hat{N}_1 + 2\hat{N}_2}{2\sqrt{3}}) \end{aligned} \tag{69}$$

- **Biaxial extension :**

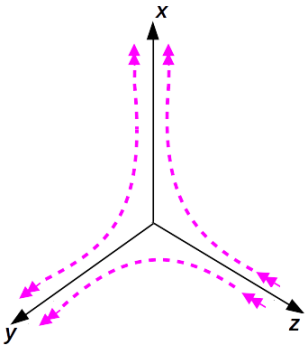

FIGURE 6: Biaxial extensional flow

In this last canonical case, the deformation rate tensor writes :

$$\mathbf{E} = \begin{pmatrix} \dot{\epsilon} & 0 & 0 \\ 0 & \dot{\epsilon} & 0 \\ 0 & 0 & -2\dot{\epsilon} \end{pmatrix} \tag{70}$$

with $\dot{\gamma} = 2\sqrt{3}\dot{\epsilon}$ so that :

$$\hat{\mathbf{E}} = \frac{\mathbf{E}}{\dot{\gamma}} = \begin{pmatrix} \frac{1}{2\sqrt{3}} & 0 & 0 \\ 0 & \frac{1}{2\sqrt{3}} & 0 \\ 0 & 0 & -\frac{1}{\sqrt{3}} \end{pmatrix} \tag{71}$$

and the total stress writes :

$$\boldsymbol{\Sigma} = -p\mathbf{I} + \eta_f \eta_s \dot{\gamma} \left(\frac{1}{\sqrt{3}} - \frac{\hat{N}_1 + 2\hat{N}_2}{6} \right) \begin{pmatrix} 1 & 0 & 0 \\ 0 & 1 & 0 \\ 0 & 0 & -2 \end{pmatrix} \tag{72}$$

The extensional viscosity is here defined as :

$$\begin{aligned} \eta_E &= \frac{\Sigma_{11} - \Sigma_{33}}{\dot{\epsilon}} \\ &= 6\eta_f \eta_s (1 - \frac{\hat{N}_1 + 2\hat{N}_2}{2\sqrt{3}}) \end{aligned} \tag{73}$$

Discussion.

The Trouton Ratio (TR) $\eta_E/(\eta_f \eta_s)$ from Eqs. (65), (69) and (73) is displayed in Fig.7 as a function of the particle volume fraction. We recall here that the TR for a Newtonian liquid is respectively respectively 3, 4, 6 for the uniaxial, planar and biaxial EF. On the whole, the suspensions behavior is quite close to that of a Newtonian liquid. In the planar EF, the predicted TR is exactly equal to the Newtonian value 4, while in the two remaining cases, the difference is due to the factor $\frac{\hat{N}_1+2\hat{N}_2}{2\sqrt{3}}$, which amounts to 0.25 at most (AnnexeA).

There are only few discrete numerical simulations in the literature concerning suspensions in EF to which we can compare this behavior. Recently, Cheal and Ness [44] have computed the extensional viscosity of non-Brownian suspensions for all three EF. They have considered two different values of the friction coefficient between particles, namely 0 and 1. In both cases, they find values of the TR close to the Newtonian value, except in the very high volume fraction range close to the jamming point. Their computed TR is reproduced in Fig.7 for frictional particles. The jamming volume fraction for their suspension in simple shear flow is 0.575, close to value $\phi_m = 0.583$ from our model. In the moderately concentrated range ($\phi \lesssim 0.56$), the computations and the predictions of our model are in good agreement. We note that Seto et al., in their paper concerning the simulations of discontinuous shear thickening of non-Brownian suspensions [43], also found that the TR for a planar EF is close to the Newtonian value 4, both for frictional and frictionless particles, in the volume fraction range that they probe ($0.5 \leq \phi \leq 0.55$), provided that the size dispersion is sufficiently strong to prevent spatial ordering that occurs otherwise in the simple shear flow of frictionless suspensions. Returning to Fig. 7, in the high volume fraction range ($\phi \geq 0.56$), the TR from the discrete simulations significantly increases as the suspension approaches the jamming point. This is shown to originate in the variation of the jamming volume fraction with the flow type for suspensions of frictional particles [44], which is connected to the flow-depending degree of anisotropy in the suspension microstructure as jamming occurs. Our model is clearly not designed to account for such TR spike, which is however restricted to nearly jammed suspensions. As a conclusion, the model/extensional simulations agreement is very satisfactory, except in the close proximity of the jamming point.

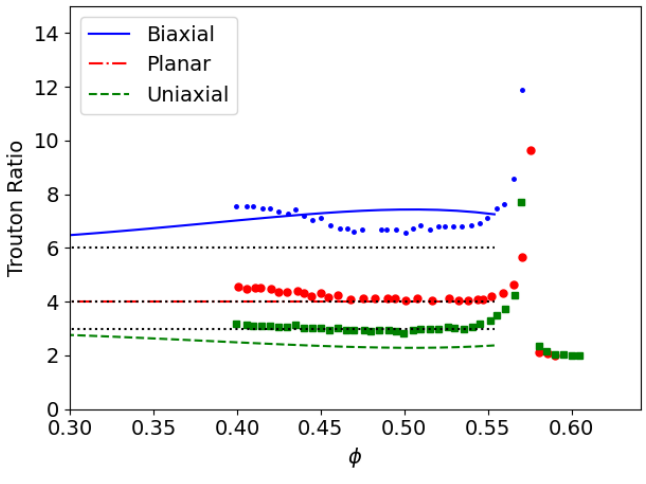

FIGURE 7: Trouton ratio as a function of volume fraction for biaxial, planar and uniaxial extensional flows. Lines : TR from the model (jamming volume fraction $\phi_m = 0.583$). Symbol : TR from discrete simulations from ref. [44] (particle friction coefficient $\mu = 1$, simple shear flow jamming volume fraction $\phi_m = 0.575$). Dotted line : TR for a Newtonian liquid.

Only few experimental studies are available in the literature to be compared to the predictions of our model. Very recently, the rheology of non-Brownian suspensions in uniaxial extensional flow was explored [63, 50], with the purpose of building a general flow model for the total stress [50] very close to Eqs. (39) and (40). Extensional flow measurements are particularly subtle, since the force on the fluid cannot be directly measured. Besides, non-Brownian suspensions show specific features that makes such experiments even more difficult : the strain-induced microstructure develops over a finite strain that is not easy to reach in experiments. In addition, the shear-viscosity of moderately concentrated non-Brownian suspensions usually displays shear-thinning behavior [64, 8]. In our attempt to build a simple model, we neglected part of those features : shear-thinning is not accounted for, nor is the transient response of the suspensions. Direct comparison with the cited experiments is thus not straightforward. However we now try to determine in what extent the present model is able to describe "real world" suspensions. From the experimental measurements in [50], both the shear and uniaxial extensional viscosities feature rate-thinning behavior. The TR is computed from the extensional viscosity at the strain rate $\dot{\epsilon}$ and the shear viscosity at shear rate $\dot{\gamma}$, with $\dot{\gamma} = \sqrt{3}\dot{\epsilon}$, i.e. for the same $||\mathbf{E}||$. The TR that they measured somewhat depends on the volume fraction in the range $0.3 - 0.5$, but the main trend concerns the variation of the TR with the elongation rate $\dot{\epsilon}$, that decreases from approximately 5 to 2 over a strain rate range $0.6 - 40s^{-1}$. The output of the present model is thus in qualitative agreement with the experimental range for the TR, even though this model is, again, essentially unable to account for the deformation rate-thinning behavior that is observed in experiments.

2.2.5. The limitations of the model

The present model has been examined in the case of classical steady flows (Sec. 2.2.2 to 2.2.4) that correspond to most of the available experimental and discrete simulations data from the literature. However, the expressions of the stresses in Eqs.(40) and (45) have quite large implications that may not be evidenced in the flows that were dealt with previously. The question arises as to what extent this model would be able to describe general suspension flows. It should be first noted that in the field of polymer rheology, the second-order fluid model is considered as a simplified version of more general models of visco-elastic fluids. In particular, it is known to conveniently account for the main rheological properties of such a fluid in slow motion and in slowly varying flow conditions [45, 56], i.e. when the flow characteristic times are much longer than the relaxation time of the fluid. In other conditions, the full visco-elastic models must be implemented.

The case of athermal suspensions of rigid particles immersed in a Newtonian fluid is quite different indeed : no elasticity or relaxation time can be evidenced, and transient experiments are explained rather in terms of typical strain than time. More precisely, the non-Brownian suspension rheology is closely connected with the so-called shear-induced microstructure that denotes the relative spatial arrangement of the particles and the force network [25, 20, 26, 21, 65]. For a given microstructure, stresses are instantaneously imposed by the inter-particle force network and the ambient strain rate [28]. Explicit modeling of this microstructure and its time (strain) evolution seems crucial to account for specific flow histories, such as shear-reversal, where stress discontinuity is observed as the shear rate is reversed [12, 66]. In that case, a structure tensor $\mathbf{S}$, akin to a fabric tensor, accounts for the shear induced microstructure [67, 68, 38, 39]. Also required are an evolution equation for $\mathbf{S}$ as well as a procedure to compute the stresses from $\mathbf{S}$ and $\mathbf{E}$.

In the present article, we follow a less ambitious purpose. The idea is to tackle "steady-like" flows, i.e. smoothly varying flows along time and space, keeping away from discontinuously varying microstructure and velocity gradients, yet accounting for relevant rheological properties,

such as anisotropic normal stresses. We found not easy to formally determine how the model that we propose may be considered a simplified version of more elaborated models based on a structure tensor. There are mainly two reasons for this : the microstructure of the suspension is strongly modified by the velocity gradients and strongly affect the stresses, so that it cannot be considered a small perturbation. In addition, in connection with the lack of material relaxation time, the microstructure adjusts to flow modifications over a typical strain of 1 to 6, depending on the solid volume fraction [12]. As a consequence, any steady simple shear flow, for which the relative angular velocity is equal to the strain rate, cannot be straightforwardly considered slow. Hence, it is not easy to define theoretically the scope of the present model. Rather, we try to bring out the flow classes for which the model seems to fit to physical reality, and the flows for which problems are expected.

Inspection of Eqs. (40) and (45) shows that the stresses depend primarily on the instantaneous value of the shear rate $\dot{\gamma}$ and of the reduced strain rate tensor $\hat{\mathbf{E}}$, the latter defining the type of considered straining flow (planar extensional, uniaxial extensional etc.). In addition, the term in $\frac{1}{\dot{\gamma}}\frac{\mathcal{D}\hat{\mathbf{E}}}{\mathcal{D}t}$ depends on the time variation of $\hat{\mathbf{E}}$ and on the vorticity tensor $\mathbf{\Omega}$. This term, which is instrumental in accounting for the first normal stress difference in simple shear flow, deserves to be discussed in more general terms. We propose to use Eq. (37) to categorize different types of flow. We note that such a categorization has been found relevant in the polymer rheology literature [61]. To this purpose, the term in $\frac{1}{\dot{\gamma}}\frac{\mathcal{D}\hat{\mathbf{E}}}{\mathcal{D}t}$ is explicitely quoted in Eq. (74) :

$$\frac{1}{\dot{\gamma}}\frac{\mathcal{D}\hat{\mathbf{E}}}{\mathcal{D}t} = \frac{1}{\dot{\gamma}}\sum_{i=1}^{3}\frac{D\hat{\xi}_i}{Dt}\mathbf{e_i}\otimes\mathbf{e_i} + \frac{\mathbf{\Delta\Omega}}{\dot{\gamma}}.\hat{\mathbf{E}} - \hat{\mathbf{E}}.\frac{\mathbf{\Delta\Omega}}{\dot{\gamma}} \qquad (74)$$

According to this classification, the flows that were considered in Sec. 2.2.2 to 2.2.4 fall into two specific categories. Firstly, the simplest case corresponds to the homogeneous steady extensional flows. Such flows define a class of flows where the strain rate tensor as seen in the frame of the moving (non-) rotating fluid is constant : the reduced principal rates $\hat{\xi}_i$ are constant in space and time, and both the fluid and eigenframe angular velocities vanish, so that $\frac{1}{\dot{\gamma}}\frac{\mathcal{D}\hat{\mathbf{E}}}{\mathcal{D}t} = 0$. This feature fits to the physical intuition : the microstructure is built by the steady straining flow, without any rotation, and the stress only depends on the volume fraction, the shear rate and the reduced strain rate tensor. In addition, in the case of a time-varying extensional flow, if the geometry, i.e. $\hat{\mathbf{E}}$, does not change, the stress is instantaneously the same as in the corresponding steady flow, as expected from a rate-independent suspension [44].

Then, according to the considered frame-invariant model, as shown in sec.2.2.3, steady cylindrical Couette and torsional parallel plate flows are completely equivalent to homogeneous steady simple shear flows. The strain rate tensor $\mathbf{E}$ together with the relative angular velocity $-\mathbf{\Delta\Omega}$ form a simple shear flow, where the strain rate and the relative rotation rate are equal. The RHS of Eq. (74) is given by the last two terms, leading to the expression in Eq.(42). In particular $\|\frac{1}{\dot{\gamma}}\frac{\mathcal{D}\hat{\mathbf{E}}}{\mathcal{D}t}\| \sim 1$. We stress again that, even in the case of an unsteady version of such flows, the first term in the RHS of Eq.(74) vanishes, and the last two terms are not modified compared to the steady case. This behaviour is thus consistent with the rate independent suspensions that are dealt with in the present study. We note that Miller et al. [35] based their model of suspension rheology in 2-D flow on this balance between strain rate and relative angular velocity.

More generally, in the frame of the present model, any homogeneous velocity gradient may be completely defined by the shear rate $\dot{\gamma}$, the reduced strain rate $\hat{\mathbf{E}} = \mathbf{E}/\dot{\gamma}$ and the reduced relative angular velocity tensor $\mathbf{\Delta\Omega}/\dot{\gamma}$. For such a flow, it appears clearly from Eqs.(74) and (34) that the ratio of the stress to the shear rate is not affected by the time-variation of the shear-rate as expected from a rate-independent material. The idea is that the microstructure originates in the competition between $\hat{\mathbf{E}}$ and $\mathbf{\Delta\Omega}/\dot{\gamma}$, and that the overall flow intensity only affects the stress level.

However, there are flows for which Eqs.(74) and (34) seem less plausible. The clearer example is maybe a homogeneous 2-D velocity gradient for which the relative angular velocity $\|\mathbf{\Delta\Omega}\|$ is much larger than the shear rate $\dot{\gamma}$. In that case, a moving fluid volume sees a rotating strain tensor at the angular velocity $\|\mathbf{\Delta\Omega}\|$: it is deformed back and forth at the frequency $2\pi/\|\mathbf{\Delta\Omega}\|$. The deformation during half a period is given by $\gamma \sim \pi\dot{\gamma}/\|\mathbf{\Delta\Omega}\| \ll 1$. According to oscillatory shear experiments [23, 14, 69], it is expected that no microstructure develops, leading to low viscosity and isotropic normal stress [70] . The present model predicts a totally different behaviour, since $\|1/\dot{\gamma}\ \mathcal{D}\hat{\mathbf{E}}/\mathcal{D}t\| \gg 1$. For instance, in the case of the superposition of a planar straining flow and a high speed angular velocity in the same plane, we get :

$$\hat{\mathbf{E}} = \begin{pmatrix} 0 & 1/2 & 0 \\ 1/2 & 0 & 0 \\ 0 & 0 & 0 \end{pmatrix} \qquad \frac{\mathbf{\Omega}}{\dot{\gamma}} = \begin{pmatrix} 0 & \omega/\dot{\gamma} & 0 \\ -\omega/\dot{\gamma} & 0 & 0 \\ 0 & 0 & 0 \end{pmatrix} \tag{75}$$

with $\dot{\gamma} \ll \omega$ yielding :

$$\frac{1}{\dot{\gamma}}\frac{\mathcal{D}\hat{\mathbf{E}}}{\mathcal{D}t} = \frac{\omega}{\dot{\gamma}} \begin{pmatrix} -1 & 0 & 0 \\ 0 & 1 & 0 \\ 0 & 0 & 0 \end{pmatrix} \tag{76}$$

The shear stress as measured in the present frame is the same as in simple shear flow, while the first normal stress difference and part of the second normal stress is proportional to $\|\mathbf{\Delta\Omega}\| \sim |\omega| \gg \dot{\gamma}$, in clear disagreement with physical sound arguments.

Even though a few examples are not sufficient to draw definitive conclusions, and keeping away from shear-reversal or cross-shear experiments, it seems that the present model may not conveniently describe flows such that $1/\dot{\gamma}$ $\|\mathcal{D}\hat{\mathbf{E}}/\mathcal{D}t\| \gg 1$, i.e. when the reduced strain rate tensor as seen by a rotating fluid volume undergoes important variations in the time required for this volume to undergo a unit deformation. This is the case when the relative angular velocity is much stronger than the strain rate or when the strain tensor type, defined by the principal values $\hat{\xi}_i$ of $\hat{\mathbf{E}}$, rapidly changes at the scale of a unit strain. Physical arguments may suggest that the stresses would lag the strain rate, due to the strain required for the microstructure to reorganize. However, definitive conclusions are difficult to draw concerning such flows, due to the lack of experimental or numerical data. We finally recall that shear-reversal or cross shear experiments fall into this category, since the reduced shear-rate tensor is instantaneously modified. In that case, obviously, the stresses do not obey the steady constitutive law, due to the finite strain required for the microstructure to reorganize. We also note that the same seems to apply in pressure-imposed experiments, when the particle pressure is abruptly modified. In such a case, the transient stress seems not to be well accounted for using the steady constitutive law, and a Reynolds-like dilatancy contribution has to be taken into account. The typical strain scale necessary to recover the steady constitutive law is again of order 1 [71].

Finally, even though the present model presumably suffers imperfections in the regime $1/\dot{\gamma}\ \|\mathcal{D}\hat{\mathbf{E}}/\mathcal{D}t\| \gg 1$ or concerning shear-reversal, it reproduces well the suspension rheological behaviour as measured in rheometrical flows, in particular anisotropic normal stresses, or extensional viscosity. In addition, it is very simply implemented in 3D Computational Fluid Dynamics (CFD) software, since it does not require explicit computing of the relative angular velocity $\mathbf{\Delta\Omega}$.

3. Numerical implementation

The model is numerically solved making use of the open source software package OpenFOAM (Open Field Operation and Manipulation). OpenFOAM is a C++ Computational Fluid Dynamics (CFD) toolbox that uses the finite volume method on a colocalized grid for the discretization

of systems of partial differential equations. The choice of this implementation is motivated by the facility of using OpenFOAM, the free access to its numerous tools and the simplicity of solver creation as its language is close to the mathematical language. In this paragraph, we will present a brief description of the discretization and resolution algorithm. For more details, one may refer to [72, 73, 74, 75].

3.1. Discretization and Resolution algorithm

We write the governing equations as they are implemented in OpenFOAM :

$$\nabla.\mathbf{u} = 0 \tag{77a}$$

$$\frac{\partial \rho_m \mathbf{u}}{\partial t} + \nabla.(\rho_m \mathbf{u} \otimes \mathbf{u}) - \nabla \cdot (\eta_f \eta_s (\nabla \mathbf{u} + \nabla \mathbf{u}^T)) = - \nabla p + \nabla.(\eta_f \eta_s \dot{\gamma} \hat{\mathbf{\Sigma}}^*) + \rho_m \mathbf{g} \tag{77b}$$

$$\frac{\partial \phi}{\partial t} + \nabla.(\phi \mathbf{u}) + \nabla.(\phi \mathbf{u_{sed}}) = -\nabla.\mathbf{J} \tag{77c}$$

where $\hat{\mathbf{\Sigma}}^*$ is the difference between the normalized total stress deviator and the shear stress :

$$\hat{\mathbf{\Sigma}}^* = 4\frac{(\hat{N_1} + 2\hat{N_2})}{2}\left(\hat{\mathbf{E}}.\hat{\mathbf{E}} - \frac{tr(\hat{\mathbf{E}}.\hat{\mathbf{E}})}{3} I\right) - \hat{N_1}\frac{1}{\dot{\gamma}}\frac{\mathcal{D}\hat{\mathbf{E}}}{\mathcal{D}t} \tag{78}$$

$\mathbf{u_{sed}}$ the sedimentation velocity :

$$\mathbf{u_{sed}} = \frac{2a^2 f(\phi)}{9\eta_f} \times (\rho_p - \rho_f)\left[\mathbf{g} - \frac{D\mathbf{u}}{Dt}\right] \tag{79}$$

$\mathbf{J}$ the particles flux due to the migration :

$$\mathbf{J} = \frac{2a^2 f(\phi)}{9\eta_f} \times \left(\nabla.(\eta_f \eta_s \dot{\gamma} \hat{\mathbf{\Sigma}}^c)\right) \tag{80}$$

with $\hat{\mathbf{\Sigma}}^c$ the normalized contact stress

$$\hat{\mathbf{\Sigma}}^c = \hat{\mathbf{\Sigma}}^c_{33}\mathbf{I} + 2\frac{\eta_c}{\eta_s}\mathbf{E} + 4\left(\frac{(\hat{\mathbf{\Sigma}}^c_{11} + \hat{\mathbf{\Sigma}}^c_{22})}{2} - \hat{\mathbf{\Sigma}}^c_{33}\right)\hat{\mathbf{E}}.\hat{\mathbf{E}} - (\hat{\mathbf{\Sigma}}^c_{11} - \hat{\mathbf{\Sigma}}^c_{22})\frac{1}{\dot{\gamma}}\frac{\mathcal{D}\hat{\mathbf{E}}}{\mathcal{D}t} \tag{81}$$

The unsteady terms is discretized using a Euler semi-implicit time scheme. Divergence terms, which include convective and non-convective terms, are discretized using the Gauss integration with linear interpolation for non-convective terms and upwind interpolation for convective terms. The laplacian term use the Gauss integration with a linear interpolation scheme for the diffusion coefficient and a corrected scheme for the surface normal gradient. For more details about interpolation schemes, one can refer to the OpenFOAM user guide.

The equations are solved by the PIMPLE pressure-velocity coupling algorithm. This algorithm is a combination of the PISO (Pressure Implicit Split Operator) and SIMPLE (Semi-Implicit Method for Pressure-Linked Equations) algorithms, adapted to transient problems [74, 75]. The principle is that at each time step, the solution is computed by solving the system of equations several times, i.e., by performing several iterations to ensure that the explicit terms of the equations converge. Once the criteria for convergence or maximum number of iterations (defined at the beginning of the calculation) are reached, the algorithm proceeds to the next time step. This allows to ignore the stability conditions (CFL condition) introduced by the explicit terms and thus be flexible in our choice of the time step.

The resolution algorithm is summarized as follow :

1. Solve the volume fraction equation
2. Update all variables depending on ϕ
3. Prediction step : solve the momentum equation to compute an intermediate velocity field.
4. Correction step :
   (a) Solve the pressure equation
   (b) Correct the velocity using the new pressure
5. Repeat the correction step nCorrectors times (nCorrectors $= 2$ is sufficient)
6. Repeat steps $1 - 5$ if there is no convergence, or the

number of iterations is less than the maximum number of iterations

7. Move to next time step

The stability of this algorithm is improved by applying under-relaxation.

3.2. Boundary conditions

OpenFoam built-in boundary conditions are used. For wall type boundary, we apply no-slip condition for the velocity and the fixedFluxPressure condition that adjusts the pressure gradient such that the flux is consistent with the velocity boundary condition. To ensure the conservation of the total volume of the particles, we impose no migration and sedimentation flux normal to the wall (slip boundary conditions in OpenFOAM) together with zero concentration gradient.

When needed in the following, other types of boundary conditions for open boundaries will be explained.

3.3. Regularization

The effective viscosity η_s (see Eq.26) diverges when $\phi \to \phi_m$. A regularization is then necessary to avoid a division by zero. We then propose the following expression :

$$\eta_s = \left(1 + \frac{\frac{5}{4}\phi}{max(1-\frac{\phi}{\phi_m}, 0.01)}\right)^2 \tag{82}$$

In order to ensure that particle migration or sedimentation stops when the volume fraction ϕ approaches ϕ_m, a regularization of the hindered settling function (Eq.11) is necessary. Two methods can be used for this. The first one consists in cancelling the hindrance function in ϕ_m. We can, for example, recall the expression proposed by Miller & Morris [76] :

$$f(\phi) = (1 - \frac{\phi}{\phi_m})(1-\phi)^{\alpha-1} \tag{83}$$

with $\alpha = 2 - 4$.

Using this function the flux stops when ϕ reaches ϕ_m. However, this expression yields values quite different from the function given in Eq. (11) over the whole volume fraction range. The second method consists in not modifying the hindrance function but adding an elastic pressure in the contact stress which becomes very large when ϕ approaches ϕ_m to counter the migration or sedimentation flux. However, this method is costly in terms of computation time. We thus propose to keep the expression in Eq. (11) while canceling the particles flux $\mathbf{J}$ when $\phi = \phi_m$.

Finally, another regularization is necessary when there is a division by $\dot{\gamma}$, as for example in $\hat{\mathbf{E}} = \mathbf{E}/\dot{\gamma}$ or in the term associated to the Jaumann derivative $-\hat{N}_1/\dot{\gamma}\, D\hat{E}/Dt$. The term $1/\dot{\gamma}$ is then replaced by $1/(\dot{\gamma}+\dot{\gamma}_\epsilon)$ with $\dot{\gamma}_\epsilon = 10^{-8}\dot{\gamma}_c$. $\dot{\gamma}_c$ is the characteristic shear rate of the flow.

4. Benchmarking

In this section, we validate our modeling and numerical resolution on several migration case studies. Three rheometrical flows will be considered first, before a more complex flow will be studied. As usual, the evolution of the volume fraction is a lot slower than the flow development, allowing to consider quasi-steady state flows. As a consequence, explicit time differentiation of the normalized strain rate tensor (first term of the RHS of Eq. (33)) is removed. It should be however noted that the terms in the expression of the stresses that involve the Jaumann time-derivative will not vanish in general due to spatial variations of the flow. Finally,to keep the paper reasonably short only the final state is studied for each case.

Concerning rheometrical flows, as pointed out in 2.2.3, the frame-invariant model yields stresses equivalent to those found in simple shear flow. Thus, for these flows, the frame-invariant model differs from the "Suspension Balance Model" [1, 2, 3, 4] only in the choice of material functions. The proposed simulations provide the opportunity to check the relevance of the material functions that we propose with respect to migration problems, as well as to validate the numerical solution against analytical solutions.

Finally, the flow through sudden expansion at low Reynolds numbers will be considered. This flow presents shear, extension or rigid-body motion regions, and cannot be tackled using the simplified (shear-flow) constitutive law for stress.

It should be noted that throughout the present section, only neutrally-buoyant particles will be considered, so that neither the gravity force nor the particle inertia plays a role in the transport of the particles (see Eqs.(77) and (79)).

4.1. Concentric Couette flow

The suspension is bounded by two concentric cylinders, where the inner cylinder rotates at an angular velocity ω, while the outer cylinder is at rest (see Fig.2). In its initial state, the suspension is uniform throughout the Couette. During flow, the particles migrate towards the outer cylinder, where the shear rate is the lowest, until reaching a stationary non-uniform concentration profile. In order to assess our numerical resolution, we calculate a semi-analytical concentration profile at steady state $\phi(r)$ and then compare it to the numerical data. This semi-analytical solution is calculated following the same procedure as Morris & Boulay [3].

In the cylindrical coordinate system (r, θ, z), the velocity is assumed here to be expressed as $\mathbf{u} = u_\theta(r)\mathbf{e}_\theta$ and volume fraction as $\phi = \phi(r)$. At steady state, and recalling that $\rho_p = \rho_f$, the volume fraction balance equation (77c) and the orthoradial component of the momentum equation (77b) may be integrated, yielding :

$$\left(\nabla.\mathbf{\Sigma^c}\right).\mathbf{e_r} = 0 \tag{84a}$$

$$\frac{1}{r^2}\frac{d\left(r^2\eta_f\eta_s\dot{\gamma}\right)}{dr} = 0 \tag{84b}$$

i.e. :

$$\frac{d\Sigma^c_{rr}}{dr} = \frac{\Sigma^c_{\theta\theta} - \Sigma^c_{rr}}{r} \tag{85a}$$

$$\dot{\gamma} = \frac{C}{r^2\eta_f\eta_s} \tag{85b}$$

where C is the constant of integration. In this flow, the basis vectors $\mathbf{e}_\theta$ and $\mathbf{e_r}$ correspond respectively to the direction of the flow and the velocity gradient (Fig.1). With the notations introduced in part 2.2, the equation (85a) writes :

$$\frac{d\left(\eta_f\eta_s\dot{\gamma}\hat{\Sigma}^c_{22}\right)}{dr} = \frac{(\hat{\Sigma}^c_{11} - \hat{\Sigma}^c_{22})\eta_f\eta_s\dot{\gamma}}{r} \tag{86}$$

Using (85b), we get then the following dimensionless expression :

$$\frac{d\hat{\Sigma}^c_{22}}{d\hat{r}} = \frac{\hat{\Sigma}^c_{11} + \hat{\Sigma}^c_{22}}{\hat{r}} \tag{87}$$

where $\hat{r} = \frac{r}{R_{out}}$. Which may be written as an ordinary differential equation (ODE) :

$$\frac{d\phi}{d\hat{r}} = \frac{\hat{\Sigma}^c_{11} + \hat{\Sigma}^c_{22}}{\hat{r}\frac{d\hat{\Sigma}^c_{22}}{d\phi}} \tag{88}$$

Eq.(88) is solved using a fourth order Runge-kutta method while imposing the constraint :

$$2\pi\int_{\frac{R_{in}}{R_{out}}}^{1}\phi(\hat{r})\hat{r}d\hat{r} = \phi_{bulk}\pi\left(1 - \left(\frac{R_{in}}{R_{out}}\right)^2\right) \tag{89}$$

This constraint imposes indeed the volume conservation of the particles.

Although the migration dynamics can be influenced by viscosity, particle size or shear rate (see Eq.(80)), Eqs.(88) and (89) show that the stationary solution only depends on the initial concentration ϕ_{bulk} and the ratio R_{in}/R_{out}. The solution of Eqs.(88) and (89) is obtained for the parameters $R_{in}/R_{out} = 2/3$ and $\phi_{bulk} = 0.40$. It is compared to the output of our numerical method in Figs. 9.

In the latter, the geometry is 2D with 90 elements in the radial direction and 140 elements in the azimuthal direction (Fig.8*a*). Boundary conditions must only be imposed at the wall, as explained in section 3.2. The volume fraction distribution across the gap is displayed in Figs. 8b and 9.

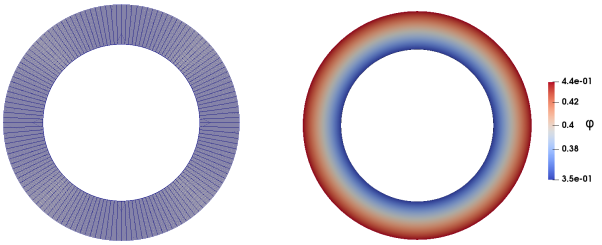

(a) (b)

FIGURE 8: Couette flow simulation : (a) 2D Couette mesh (b) Numerical volume fraction distribution at steady state.

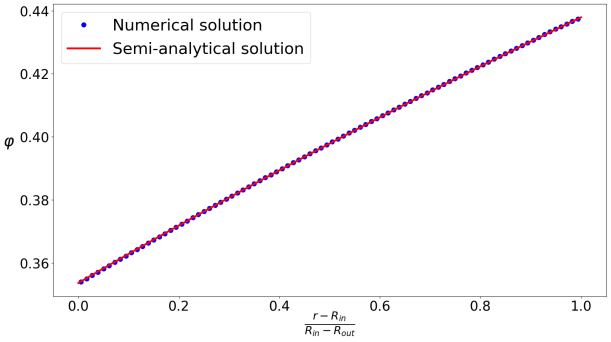

FIGURE 9: Radial concentration profile at the steady state for a concentric Couette flow : comparison between the semi-analytical solution and the numerical solution for $\phi_{bulk} = 0.40$.

As shown in Fig.9, the numerical and semi-analytical results are in good agreement, confirming that Eqs. (77a)-(81) are conveniently tackled by the present numerical method.

We will then compare the data from our model to the recent experimental measurements of Sarabian et al. [77]. The dimension of the Couette is $R_{out} = 60\ mm$ and $R_{in}/R_{out} = 2/3$ as before. Particles are rigid Polymethylmetacrylate (PMMA) spheres with a radius of $a = 0.79\ mm$ and a density of $\rho_p = \rho_f = 1190\ kg.m^3$. The suspending fluid is a viscous mixture composed of Triton X-100, zinc chloride, water and hydrochloric acid with a viscosity of $\eta_f = 4.64\ Pa.s$. The experiment was carried out for different initial concentrations ϕ_{bulk} (0.2, 0.3, 0.35, 0.4, 0.45, 0.5) .

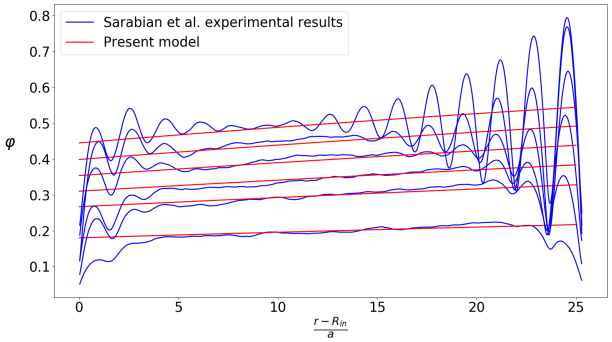

FIGURE 10: Radial concentration profile at the steady state for different initial concentrations ($\phi_{bulk} = 0.2, 0.3, 0.35, 0.4, 0.45, 0.5$) : comparison with the experimental results of Sarabian et al.[77]

As shown in Figure 10, the model results are consistent with the experimental measurements of Sarabian et al. [77]. The significant oscillations in the experimental measurements are caused by the particle partial ordering of the suspension close to the boundaries. Obviously, this layering cannot occur in the continuous medium modeling that is considered in the present paper. In spite of this, the steady volume fraction profiles from the experiments and from the numerical computation are in quite satisfactory agreement.

4.2. Pipe flow

The suspension now flows under the action of an axial pressure drop applied to the extremities of a cylindrical tube of radius R, the axis direction of which is denoted by $\boldsymbol{e}_z$. None of the quantities, except for the pressure, is supposed to depend on the z-coordinate. In its initial state, the suspension is uniform throughout the tube section. During flow, shear-induced particle migration occurs towards the axis of the tube where the shear rate is zero. As in the previous section, we want to validate the numerical resolution by comparing to a semi-analytical solution. In the cylindrical coordinate system (r, θ, z), the steady solution is to be sought in the form $\boldsymbol{u} = u(r)\boldsymbol{e}_z$ for the velocity and $\phi = \phi(r)$ for the volume fraction. The flow is locally a simple shear flow in the usual meaning, and $\boldsymbol{e}_r$ and $\boldsymbol{e}_\theta$ correspond respectively to the direction of the velocity gradient and the vorticity. Eq. (77c) and the z-component of

Eq.(77b) reduce to :

$$\frac{d\left(\eta_f \eta_s \dot{\gamma} \hat{\Sigma}^c_{22}\right)}{dr} = \frac{(\hat{\Sigma}^c_{33} - \hat{\Sigma}^c_{22})\eta_f \eta_s \dot{\gamma}}{r} \tag{90a}$$

$$\dot{\gamma} = \frac{-\nabla P_z}{2\eta_f \eta_s} r \tag{90b}$$

∇P_z is the axial pressure gradient. Eqs.(90a) and (90b) yield the following dimensionless expression :

$$\frac{d\hat{\Sigma}^c_{22}}{d\hat{r}} = \frac{\hat{\Sigma}^c_{33} - 2\hat{\Sigma}^c_{22}}{\hat{r}} \tag{91}$$

where $\hat{r} = \frac{r}{R}$. Eq.(91) may be written as an ODE :

$$\frac{d\phi}{d\hat{r}} = \frac{\hat{\Sigma}^c_{33} - 2\hat{\Sigma}^c_{22}}{\hat{r}\frac{d\hat{\Sigma}^c_{22}}{d\phi}} \tag{92}$$

Furthermore, we can observe that this equation has a singularity due to the factor $1/\hat{r}$ in the RHS. Since the expression $(\hat{\Sigma}^c_{33} - 2\hat{\Sigma}^c_{22})/\frac{d\hat{\Sigma}^c_{22}}{d\phi}$ does not vanish as the volume fraction tends to the jamming volume fraction ϕ_m, $d\phi/d\hat{r}$ diverges as $\hat{r}$ tends to zero. Actually, the value $\phi = \phi_m$ is not associated with any specific property of the mentioned function, so that nothing prevents ϕ to exceed ϕ_m. A simple mathematical analysis shows that ϕ reaches ϕ_m for a value $\hat{r}_J \in]0, 1]$ no matter how low the value of ϕ at $\hat{r} = 1$ (see also ref. [78] for the same statement with different material functions). For this reason, in our two-dimensional numerical solution, the flux at one face is set to zero when it tends to increase the volume fraction of the adjacent cell if it is equal to ϕ_m (see section 3.3). The equivalent here for the semi-analytical resolution method corresponds to defining a radius R_j separating the flow region from the jamming. Thus, in the region of radius R_j, the concentration is ϕ_m while for the region between R_j and R, the concentration verifies the Eq.(92). The value of R_j is determined by satisfying the conservation of the total particle volume, i.e. :

$$2\pi \int_{\frac{R_j}{R}}^{1} \phi(\hat{r})\hat{r}d\hat{r} + \phi_m \pi \left(\frac{R_j}{R}\right)^2 = \phi_{bulk}\pi \tag{93}$$

Eq.(92) is solved using fourth order Runge-kutta method and we compare the output data to our numerical solution for $\phi_{bulk} = 0.40$. The governing equations are solved over a disc, one mesh element wide in the axial direction. An axial pressure gradient is added to the momentum equation, that drives the flow, and cyclic (i.e. periodic) conditions are imposed at input and output boundaries. The boundary conditions on the outer wall have been discussed in section 3.2. The radial mesh size is not uniform (see Fig.11a) : in the region $r < 0.3R$, where the solution is stiff, we define a space step of $\Delta r = 6.5\ 10^{-3} R$ and then from $r = 0.3R$, this radial step increases with an amplification rate of 1.02 up to $\Delta r = 2.0\ 10^{-2} R$.

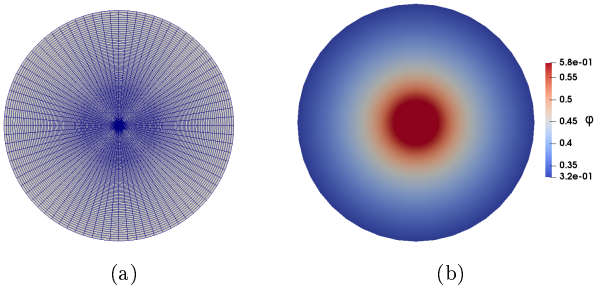

(a) (b)

FIGURE 11: Pipe flow simulation : (a) 2D pipe mesh (b) Numerical volume fraction distribution at the steady state.

Figure 12 shows a good agreement between the concentration profiles from the 2D computation and the 1D semi-analytical solution.

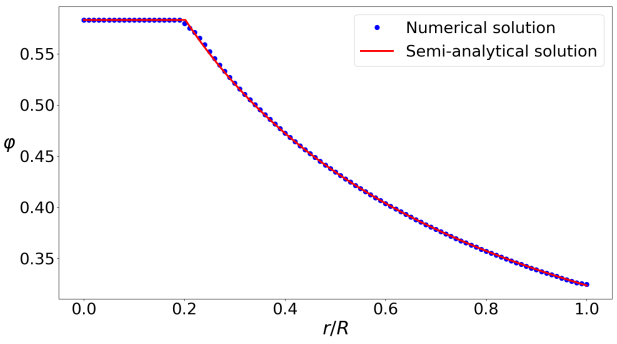

FIGURE 12: Radial concentration profile at the steady state for a pipe flow : comparison between the semi-analytical solution and the numerical solution for $\phi_{bulk} = 0.40$.

We now compare our model to the experimental measurements of Snook et al. [78]. The particles used are PMMA

spheres with a diameter of $2a = 2.01\ mm$ and a density of $\rho_p = 1190\ kg.m^{-3}$. The suspending fluid, composed of $ZnCl_2$, water and Triton X-100, is chosen so that its density is equal to the density of the particles. The experimental device is a glass tube of length 46.8 cm and diameter $2R = 1.65\ cm$. The comparison is carried out for two initial concentrations $\phi_{bulk} = 0.3$ and $\phi_{bulk} = 0.4$.

(a) $\phi_{bulk} = 0.3$

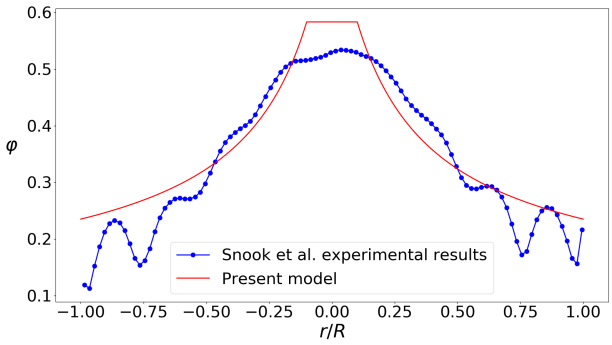

(b) $\phi_{bulk} = 0.4$

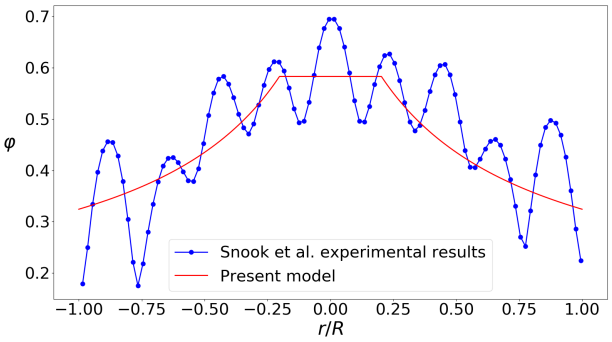

FIGURE 13: Radial concentration profile at the steady state for : (a) $\phi_{bulk} = 0.3$ and (b) $\phi_{bulk} = 0.4$. Comparison with the experimental results of Snook et al.[78].

The results (Fig.13) are overall in good agreement. According to Snook et al.[78], the oscillations that can be observed on the experimental measurements, in particular for $\phi_{bulk} = 0.4$, are the layers of particles due to the high level of confinement. These oscillations cannot be observed with the present model since it is a continuous medium model.

Then, we are interested in the discrete numerical simulations of Yeo et al. [79]. The device is an infinite channel of half gap h. The simulations were performed for ratios of $\frac{h}{a} = 9$, $\frac{h}{a} = 12$ and initial concentrations of $\phi_{bulk} = 0.3$, $\phi_{bulk} = 0.4$. In Figure 14, the results of Yeo et al. are compared to those of the present model at the steady state. As can be seen, the results are in good agreement. Again, contrary to the present model, the discrete simulations show the influence of confinement at the boundary. We can also note a difference for $\phi_{bulk} = 0.3$, where contrary to this model, the experimental measurements of Snook et al.[78] and the discrete simulations of Yeo et al.[79] do not reach the jamming ($\phi_m = 0.583$). Indeed, the "Suspension Balance Model" from which our model is inspired predicts jamming of the suspension because of the above mentioned singularity whatever the bulk volume fraction. It is a important limitation of the Suspension Balance Model. This can be avoided by introducing a non-local shear rate [5][78] [76], but at the cost of a non physical cusp-like shape at the center r = 0. However, this issue requires further investigation which is out of scope of this article.

(a) $\phi_{bulk} = 0.3$

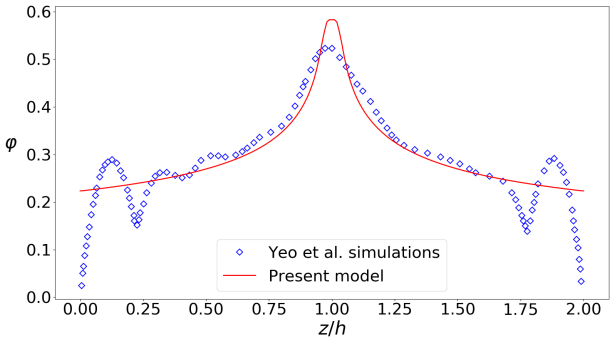

(b) $\phi_{bulk} = 0.4$

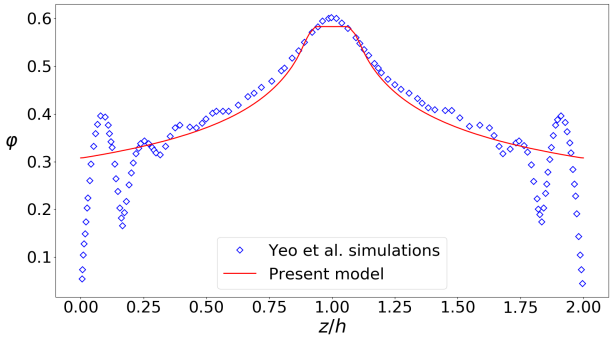

FIGURE 14: Radial concentration profile at the steady state for : (a) $\phi_{bulk} = 0.3$, $\frac{h}{a} = 9$ and (b) $\phi_{bulk} = 0.4$, $\frac{h}{a} = 12$. Comparison with the discrete simulations of Yeo et al. [79].

4.3. Torsional parallel plate flow

In this part, we study a suspension flow between two parallel discs of radius R separated by a distance h. The upper disc rotates with an angular velocity ω, while the lower disc is held fixed (see Fig.3). In the initial state, the suspension is uniform throughout the geometry. The radial particles migration of this flow remains an open problem. Indeed, studies (modeling or experiments) diverge on this subject. Some describe an absence of migration, others an outward migration or even an inward migration. This question is not yet settled. The reader may refer to [80] [81] for more details on this topic. We will see later that the model presented here predicts outward or inward migration depending on the initial concentration.

We determine the semi-analytical solution. We consider the natural cylindrical basis ($\mathbf{e_r}$, $\mathbf{e}_\theta$, $\mathbf{e_z}$). In a Newtonian fluid, inertia causes secondary flows in the r-z plane as soon as the Reynolds number $Re = \rho_f \omega h^2/\eta_f$ is non-zero [82, 83]. In the following, for the calculation of the semi-analytical solution, we assume Re = 0, so that recirculation flows are absent, i.e. the velocity field is torsional $\mathbf{u} = \frac{\omega r z}{h}\mathbf{e}_\theta$. The shear rate expression can then be determined (see Sect.2.2.3) :

$$\dot{\gamma} = \frac{\omega r}{h} \tag{94}$$

As can be seen, the shear rate here depends only on r, therefore the migration can only be radial : $\phi = \phi(r)$. By noting that $\mathbf{e}_\theta$ and $\mathbf{e_r}$ correspond here respectively to the directions of velocity and vorticity (directions 1 and 3 in Fig. 1), the particle volume conservation equation (Eq.(77c)) reduces in steady state to :

$$\frac{d\left(\eta_f \eta_s \dot{\gamma} \hat{\Sigma}^c_{33}\right)}{dr} = \frac{(\hat{\Sigma}^c_{11} - \hat{\Sigma}^c_{33})\eta_f \eta_s \dot{\gamma}}{r} \tag{95}$$

Using the shear rate expression (Eq.(94)) , we derive in dimensionless form ($\hat{r} = r/R$) the following ODE :

$$\frac{d\phi}{d\hat{r}} = \frac{\left(\hat{\Sigma}^c_{11} - 2\hat{\Sigma}^c_{33}\right)\eta_s}{\hat{r}\frac{d\eta_s \hat{\Sigma}^c_{33}}{d\phi}} \tag{96}$$

We can note that contrary to the case of the Poiseuille flow where a treatment of the singularity was necessary, here, in spite of the presence of the factor $1/\hat{r}$, the right-hand side member of the Eq.(96) always converges to 0 when ϕ approaches 0 or ϕ_m (see the expressions of the material functions Sect.2.2.1). Thus, the volume fraction will remain between its boundary values 0 and ϕ_m. The ODE (96) is solved by considering the conservation of particle volume :

$$2\pi \int_0^1 \phi(\hat{r})\hat{r}d\hat{r} = \phi_{bulk}\pi \tag{97}$$

This semi-analytical solution is then compared to the numerical solution for the parameters $\phi_{bulk} = 0.3$, $h/R = 0.08$ and $Re = 0.026$. The mesh is here $3D$ and non-uniform (Fig.15a) : in the region $r < 0.28R$, we define a radial space step of $\Delta r = 4.68\ 10^{-3}R$ and then from $r = 0.28R$, this radial step increases with an amplification rate of 1.02 up to $\Delta r = 1.88\ 10^{-2}R$. The vertical space step in the gap is $\Delta z = 5.33\ 10^{-3}R$. For the velocity field boundary conditions, the upper disk is rotating around its axis while the lower disk is immobile. For the outer wall, a slip condition is applied (see section 3.2 for the boundary conditions of the other variables).

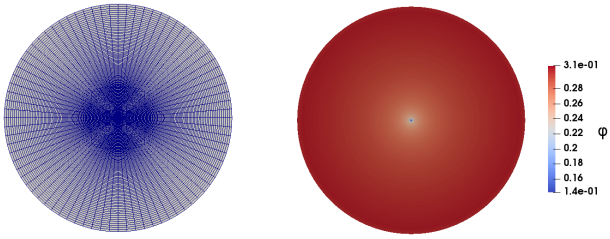

(a) (b)

FIGURE 15: Torsional flow simulation : (a) Disk mesh (b) Numerical volume fraction distribution at the steady state.

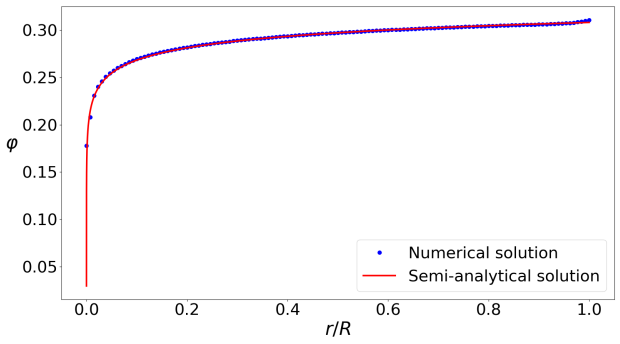

FIGURE 16: Radial steady-state concentration profile for a torsional flow : comparison between the semi-analytical solution and the numerical solution for $\phi_{bulk} = 0.3$.

As shown in figure 16, the solutions obtained are in good agreement. Also, we can observe that the result of this $3D$ simulation with a $\phi_{bulk} = 0.3$ (Fig.15b , Fig.16) shows us an outward migration with a particles-free region in the center. As noted previously, this model predicts outward or inward migration depending on the initial concentration. Indeed, as we can see from equation (96), the migration depends on the sign of $(\hat{\Sigma}^c_{11} - 2\hat{\Sigma}^c_{33})$ since all normalized contact stresses $\hat{\Sigma}^c_{ii}$ are negative and increasing in absolute value with ϕ (see AnnexeA). Thus, if $\frac{\hat{\Sigma}^c_{33}}{\hat{\Sigma}^c_{11}} < \frac{1}{2}$, the migration is outward while for $\frac{\hat{\Sigma}^c_{33}}{\hat{\Sigma}^c_{11}} > \frac{1}{2}$, the migration is inward. For $\frac{\hat{\Sigma}^c_{33}}{\hat{\Sigma}^c_{11}} = \frac{1}{2}$, there is no migration, which happens in the present model for a concentration near 0.39. In Figure 17, we plot the radial concentration profiles of the present model for different initial concentrations. Thus, it can be observed that for low concentrations, there is outward migration with a particles-free region in the center. While for high concentrations, there is no migration or little inward migration.

It is difficult to compare our numerical simulations with experimental measurements since few quantitative measurements have been made for this flow. But, we can quote the experiments of Kim et al. [84] where he studies the migration between two disks of radius 25 mm for initial concentrations $\phi_{bulk} = 0.1, 0.15, 0.2, 0.25$. They then observe an outward migration with a particles-free region in the center. Also concerning large concentrations, we can quote the experiments of Chapman [85] and Chow et al.[16] which show that the migration is weak or zero. All these experiments are in qualitative agreement with our results of figure 17. Thus, as a conclusion of this section, we can consider that our model is fully adequate to handle 3D torsional flows.

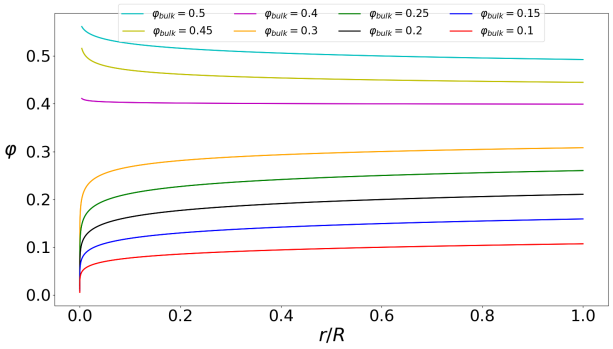

FIGURE 17: Radial steady-state concentration profiles of the present model for different initial concentrations.

4.4. Suspension flow through an abrupt expansion

As a last validation, a flow through an abrupt expansion is considered (Fig.18). This flow is more complex than those treated previously : a recirculation zone appears, and the intensity of the relative angular velocity $\frac{\mathbf{\Omega} - \mathbf{\Omega_E}}{\dot{\gamma}}$ varies from a position to another, so that there are at the same time zones of simple shear, elongational flow, and rigid body motion. As a consequence, this flow is well suited to the validation of general flow modelling. The same type of flow was tackled by Miller et al. [35] with the same purpose in planar geometry while we deal with axisymmetric geometry.

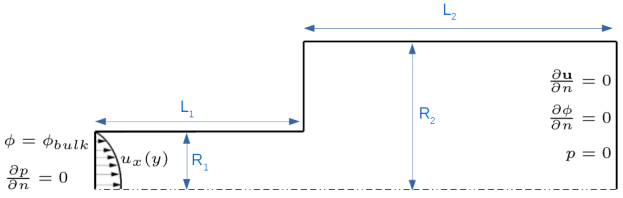

FIGURE 18: Sketch of flow geometry with the boundary conditions

The result of our numerical simulations will be compared to the experimental measurements of Moraczewski et al. [86]. Their experiment consists of a flow of a concentrated

suspension undergoing steady flow in an abrupt axisymmetric $1:4$ expansion, i.e $\frac{R_2}{R_1}=4$. The upstream tube has a radius of $R_1=0.238\ cm$ and a length of $L_1=61\ cm$ while the downstream tube has a radius of $R_2=0.955\ cm$ and a length of $L_2=1.52\ m$. In order to reduce the calculation time, we work on a wedge geometry (2D axisymmetric geometry) and reduce the length of the downstream tube. The geometry contains 25680 meshes and Fig.19 presents the mesh near the expansion. For the boundary conditions (see Fig.18), at the inlet, we impose a parabolic profile for the velocity, the concentration is fixed at ϕ_{bulk} while the pressure is set to zerogradient. At the outlet, we impose a zero pressure and a zerogradient condition for the velocity and the concentration. The boundary conditions on the outer wall have been discussed in section 3.2.

This flow requires several regularizations already presented in section 3.3. The regularisation of $\dot{\gamma}$ deserves a special attention. In the vicinity of the tube axes where $\dot{\gamma}$ tends to zero, $1/\dot{\gamma}$ must be replaced by $1/(\dot{\gamma}+\dot{\gamma}_\epsilon)$. Too small a $\dot{\gamma}_\epsilon$ increases the $(\mathbf{u}.\nabla)\hat{\mathbf{E}}$ term (Eq.(33)), introducing numerical oscillations. We have chosen to take $\dot{\gamma}_\epsilon=0.03\dot{\gamma}_c$ with $\dot{\gamma}_c=U_1/R_1$ for the upstream tube and U_2/R_2 for the downstream tube. U_1 and U_2 are the average velocities in the upstream and downstream tubes. The discontinuity of $\dot{\gamma}_\epsilon$ at the expansion point does not raise any particular problem : the shear rate does not vanish there due to the extensional flow that develops at this position.

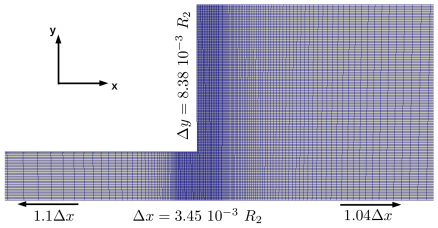

FIGURE 19: Computational mesh for a expansion geometry : The vertical space step is $\Delta y = 8.38\ 10^{-3}\ R_2$. Between $x = 63.77\ R_2$ and $x = 63.98\ R_2$, the horizontal space step is $\Delta x = 3.45\ 10^{-3}\ R_2$. Then, it increases with a ratio of 1.04 (for $x > 63.98\ R_2$) and 1.1 (for $x < 63.77\ R_2$).

First, before comparing our results with those of Moraczewski et al., we will describe the kinematics of this flow. Indeed, in this flow, the suspension can be subjected to pure extension, simple shear or even solid-body rotation. The classification of the type of flow will be done using the criterion introduced by Ryssel and Brunn [87] [35] :

$$\chi = \frac{2\|\mathbf{\Delta\Omega}\|}{\frac{\dot{\gamma}}{2}+\|\mathbf{\Delta\Omega}\|} \tag{98}$$

with $\mathbf{\Delta\Omega}=\mathbf{\Omega}_F-\mathbf{\Omega}$, the relative angular velocity. It must be recalled that the model studied here does not require the calculation of the angular velocity $\mathbf{\Omega}_F$. However, we need it for the description of the kinematics (Eq.(98)). We will therefore calculate it using the method proposed by Zhong-Heng et al. [88]. Thus, $\chi\to 0$ would correspond to a pure extension, $\chi\to 1$ to a simple shear and $\chi\to 2$ (i.e. $\dot{\gamma}\ll\|\mathbf{\Delta\Omega}\|$) to a solid-body rotation. We represent on Fig.20 this criterion for volume fractions of $\phi_{bulk}=0$, $\phi_{bulk}=0.4$ and for a Reynolds number of $Re=1.1$. The Reynolds number is based on the flow in the downstream tube : $Re=\frac{\rho R_2 U_2}{\eta_f \eta_s(\phi_{bulk})}$.

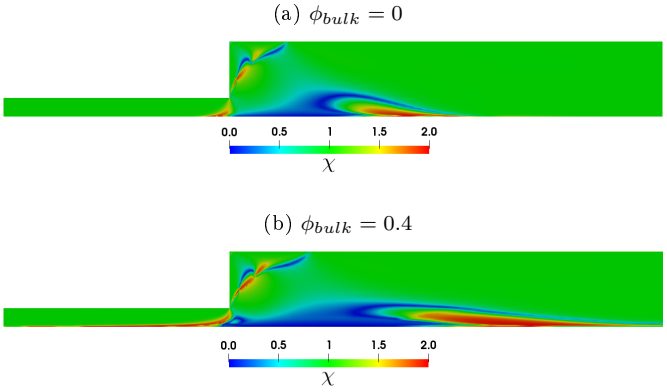

FIGURE 20: Flow classification with the χ criterion for a Reynolds number $Re=1.1$. The inlet concentration is 0 for (a) and 0.4 for (b).

Thus, it can be observed (Fig.20) that the flow is essentially a simple shear flow ($\chi\to 1$), except near the expansion. Indeed, just after the expansion, near the symmetry axis, we observe a pure extension zone ($\chi\to 0$) corresponding to the deceleration of the incoming suspension in the large tube. Upstream and downstream of this zone ap-

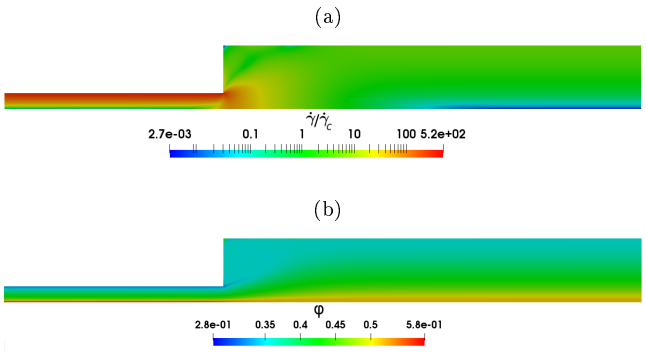

FIGURE 21: Log-scale normalized (by $\dot{\gamma}_c = \frac{U_2}{R_2}$) shear-rate (a) and concentration distribution (b) near the expansion for $\phi_{bulk} = 0.4$ and $Re = 1.1$.

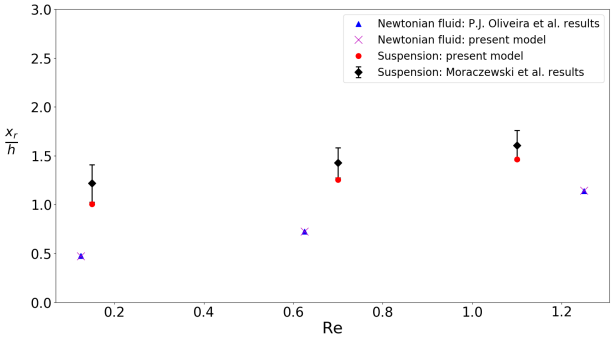

FIGURE 22: Normalized recirculation length $\frac{x_r}{h}$ as a function of the Reynolds number Re, with $h = R_2 - R_1$. Comparison to P.J. Oliveira et al. [89] results (for $\phi_{bulk} = 0$) and Moraczewski et al. results [86] (for $\phi_{bulk} = 0.4$)

pear solid-body rotation zones ($\chi \to 2$) where the rotation rate is larger than the strain rate. Indeed, near the axis in the shear zones, the extensional (resp. compressional) principal strain rate axis is oriented with respect to the tube axis at an angle of $\frac{\pi}{4}$ (resp.$-\frac{\pi}{4}$), why it is oriented perpendicular (resp. parallel) to it in the expansion zone. The regions where $\chi \to 2$ near the axis therefore correspond to the rotation of the eigenbasis of $\hat{\mathbf{E}}$ when moving from one region to the other. Finally, in the corner, where the recirculation is located, there is a mixture of pure extension and solid-body rotation zones. Also, it should be noted that all non simple shear zones are larger in a suspension (Fig.20b) than in a Newtonian fluid (Fig.20a). In Fig.21, we present the volume fraction and shear rate cartography near the expansion. We then observe that the volume fraction is roughly the image of the shear rate distribution. The highly concentrated areas correspond to the areas with the lowest shear rate. On the other hand, the migration is more important in the small tube where the shear rate gradient is higher.

Moraczewski et al. [86] measured the recirculation length x_r located after the expansion for different Reynolds numbers, particle radius of $a = 42.5\ \mu m$ and volume fraction of 0.4. Their results are compared with those of the present model in Fig.22. In this figure, the recirculation length for a Newtonian fluid is also represented and compared to the numerical simulations of P.J. Oliveira et al. [89]. As it can be seen, the results are in good agreement. This validates the present model in a general flow.

Returning to the assumption of "slowly varying flow", we measured the $\frac{1}{\dot{\gamma}}\|\frac{\mathcal{D}\hat{\mathbf{E}}}{\mathcal{D}t}\|$ term and found it to be high ($\lessapprox 25$) in regions where $\chi \simeq 2$, which is consistent with what was discussed in Section 2.2.5 about the limitations of the model. Questions then arise about the relevance of this component of the constraint. While it is difficult to estimate the quantitative influence of the assumed error, there are arguments that the influence of these terms in the stresses have a limited impact on the suspension flow and particle migration in this case. In the recirculation zone, the χ intensity distributions in the pure liquid and suspension cases are very similar, suggesting that the flow structure is the same in both cases. Furthermore, no rapid variation in concentration is observed at the spatial scale of χ variation. In the vicinity of the axis, again, the distribution of χ in the pure liquid is similar to that observed in the suspension, although the corresponding zone is larger in the latter case. However, other important factors may be responsible for this discrepancy, in particular the heterogeneous distribution of volume fraction and thus of viscosity in the case of the suspension. Concerning migration, there is also no abrupt change in volume fraction correlated with high χ values. Therefore, even though some regions of the

flow have values of $\frac{1}{\dot{\gamma}}\|\frac{\mathcal{D}\hat{\mathbf{E}}}{\mathcal{D}t}\|$ significantly larger than 1, it is likely that its influence remains small in the considered flow.

5. Conclusion

In this paper, rheological modeling of non-Brownian suspensions is proposed, that is well suited to general flows, including those that significantly differ from simple-shear flow. Balance equations are derived from the two-phase modelling. Assuming that the relative velocity of the two phases may be neglected compared to the average velocity in all inertial terms allows us to simplify the system, and to describe the suspension as a single incompressible continuous phase. Particle transport with respect to the mean suspension flow is driven by a drift velocity, which is expressed, in particular, as a function of the particle phase stress. Overall, the final governing equations are quite similar to the Suspension Balance Model [49, 4]. The main assumption regarding inertia has been checked for all flows presented in the article, making of the present mixture model a physically sound and computationally effective model.

Regarding the stress modeling, a frame-invariant formulation is proposed, that is inspired by the second-order fluid in polymer rheology. The expression of the suspension and contact stresses only involve the particle volume fraction, the generalized shear rate of the suspension flow, its reduced strain rate tensor and the Jaumann derivative of the latter. The proposed modeling is consistent with the simplified behaviour of non-Brownian suspension in steady flows : neglecting rate-dependence in simple-shear flow, it still accounts for the anisotropic normal stresses. Only four parameters for the contact stress, and three for the suspension stress, all depending only on the particle volume fraction, have to be determined. This is readily done using correlation laws from particle scale simulation of non-Brownian suspensions in simple shear flow. The modeling is shown to be consistent with the standard flow aligned modeling of non-Brownian suspension in various rheometrical shear or pressure-driven flows, and in good agreement with particle scale simulations of steady extensional flows.

The numerical implementation is performed by the finite volume method using the open-source toolbox OpenFOAM. It is validated, as well as the chosen material functions, against computation of suspension steady flow, including particle migration, in various standard geometries. The steady velocity and volume fraction profiles are in close agreement to semi-analytical solutions, and compare well with available experimental measurements and particle scale simulations from the literature. Finally, the case of the abrupt expansion of a planar pressure-driven flow is considered, and some outputs of the model are compared to experimental measurements. The flow turns out to be very complex, showing different flow type depending on location, from purely extensional flow to nearly rigid body motion, and it is properly tackled by the numerical method.

Several important limitations of the proposed modelling may be noted. Firstly, the model is expected to perform worse in cases where the Jaumann derivative of the reduced strain-rate tensor is large compared to the shear-rate, meaning that the moving and rotating fluid particle feels time-variation of this tensor faster that deformation. Since the reduced strain-rate tensor determines the steady micro-structure, and that the strain required for the micro-structure to adapt to new flow conditions is typically one, it means that the model cannot tackle important variation of the micro-structure over a strain smaller than typically one. This is the case in shear-reversal experiments, excluded from the present study, and for which the reduced shear-rate is instantaneously modified. This should be also the case for nearly rigid body motion of the suspension, where the relative rotation-rate is large compared to the shear-rate, and more generally for heterogeneous flows along which the reduced strain rate tensor rapidly evolves.

A second limitation may be observed. The accent has been put on the frame-invariant generalization of the standard constitutive functions broadly used in the different versions of the Suspension Balance Model. In particular, the stresses are proportional to the shear-rate, so that the well known drawbacks of such a modeling are to be found in the present work. More specifically, in the pressure-driven flow, the volume fraction is allowed to exceed the jamming volume fraction ϕ_m at the vicinity of the tube axis, which is observed no matter how low the average volume fraction in the tube. We chose the simplest expedient to keep the volume fraction lower than ϕ_m, i.e. artificially canceling the fluxes. Such an expedient has been recently used in a more rigorous computational way in the frame of two-phase flows using a particle phase pressure that acts as a Lagrange multiplier field [90], or in the context of a similar mixture model based on the μ-rheology [91]. We note that in the latter article, a refinement of the model allows further compression of the jammed plug, inline with some recent experimental measurements [92]. Such upgrades are only partly satisfactory though, since the volume fraction is still allowed to reach the jamming volume fraction no matter how low the mean volume fraction in the tube, contrary to what is observed in experiments. It has often been proposed to add a non-local term in the particle stress [1, 93, 76, 94, 95] to correct the latter discrepancy. Although not implemented in the present paper, the mentioned refinements may be easily included in the proposed modeling.

Finally, despite the mentioned limitations, among which some may be easily corrected, the proposed model seems a powerful generalization to general flows of the standard Suspension Balance Model. It involves a smaller number of unknown fields as in the primary two-phase model, which implies limited computational cost. The frame invariant constitutive law involves a small number of free parameters, all of which are found from shear-flow simulations. In addition, it is easily included in flow computation codes.

Acknowledgments

This work was supported by the French government, through the UCAJEDI Investments in the Future project managed by the National Research Agency (ANR) under reference number ANR-15-IDEX-01. The authors are grateful to the OPAL infrastructure from Université Côte d'Azur and the Université Côte d'Azur's Center for High-Performance Computing for providing resources and support.

AnnexeA. Material functions in simple shear flow

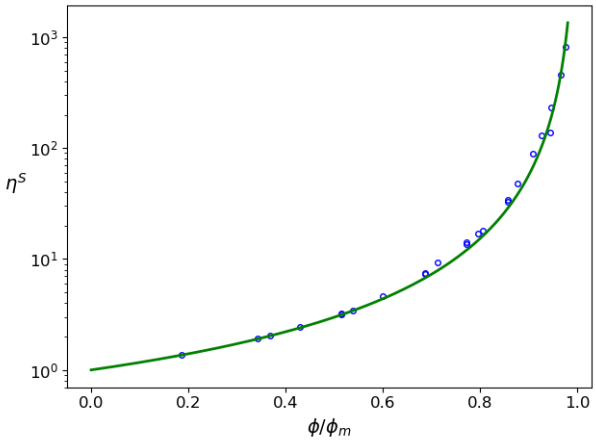

Figure A.23

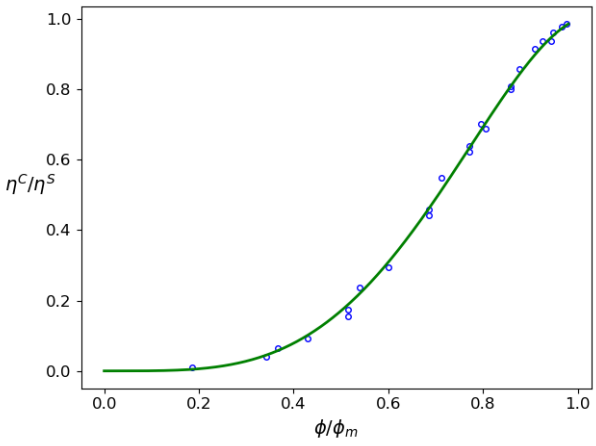

Figure A.24

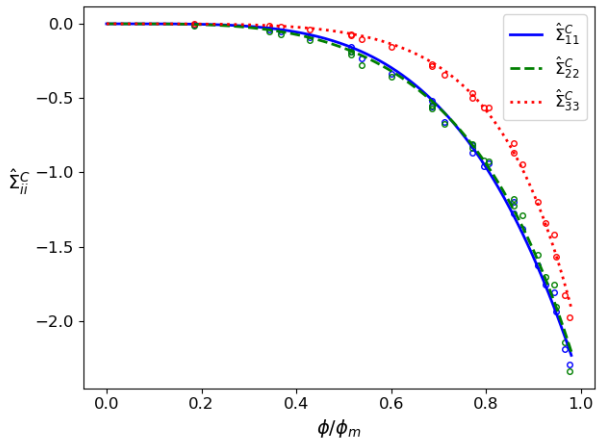

FIGURE A.25

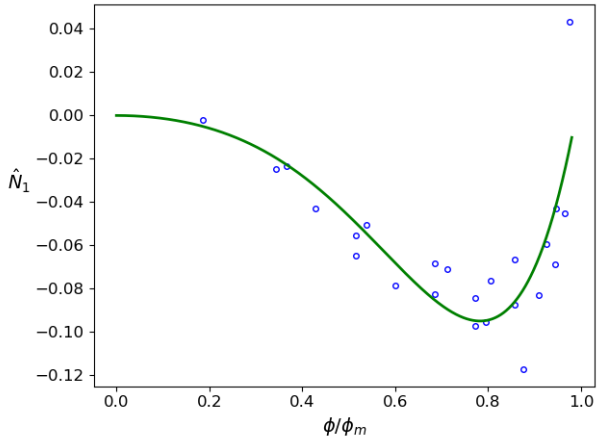

FIGURE A.26

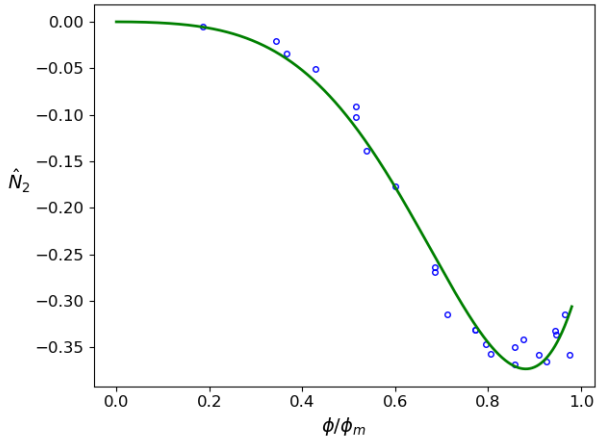

FIGURE A.27

[1] P. R. Nott, J. F. Brady, Pressure-driven flow of suspensions : simulation and theory, Journal of Fluid Mechanics 275 (1994) 157–199. doi :10.1017/S0022112094002326.

[2] P. Mills, P. Snabre, Rheology and structure of concentrated suspensions of hard spheres. shear induced particle migration, Journal de Physique II 5 (10) (1995) 1597–1608.

[3] J. Morris, F. Boulay, Curvilinear flows of noncolloidal suspensions : The role of normal stresses, Journal of Rheology 43 (1999) 1213. doi :10.1122/1.551021.

[4] P. R. Nott, E. Guazzelli, O. Pouliquen, The suspension balance model revisited, Physics of Fluids 23 (4) (2011) 043304. doi :10.1063/1.3570921.

[5] E. Guazzelli, O. Pouliquen, Rheology of dense granular suspensions, Journal of Fluid Mechanics 852 (2018) P1.

[6] F. Gadala-Maria, A. Acrivos, Shear-induced structure in a concentrated suspension of solid spheres, Journal of Rheology 24 (6) (1980) 799–814.

[7] G. Chatté, J. Comtet, A. Niguès, L. Bocquet, A. Siria, G. Ducouret, F. Lequeux, N. Lenoir, G. Ovarlez, A. Colin, Shear thinning in non-Brownian suspensions, Soft matter 14 (6) (2018) 879–893.

[8] L. Lobry, E. Lemaire, F. Blanc, S. Gallier, F. Peters, Shear thinning in non-Brownian suspensions explained by variable friction between particles, Journal of Fluid Mechanics 860 (2019) 682–710.

[9] M. M. Denn, J. F. Morris, D. Bonn, Shear thickening in concentrated suspensions of smooth spheres in Newtonian suspending fluids, Soft matter 14 (2) (2018) 170–184.

[10] I. E. Zarraga, D. A. Hill, D. T. Leighton Jr, The characterization of the total stress of concentrated suspensions of noncolloidal spheres in Newtonian fluids, Journal of Rheology 44 (2) (2000) 185–220.

[11] F. Blanc, F. Peters, E. Lemaire, Local transient rheological behavior of concentrated suspensions, Journal of Rheology 55 (4) (2011) 835–854. doi :10.1122/1.3582848.

[12] F. Peters, G. Ghigliotti, S. Gallier, F. Blanc, E. Lemaire, L. Lobry, Rheology of non-Brownian suspensions of rough frictional particles under shear reversal : a numerical study, Journal of rheology 60 (4) (2016) 715–732.

[13] J. M. Bricker, J. E. Butler, Oscillatory shear of suspensions of noncolloidal particles, Journal of rheology 50 (5) (2006) 711–728.

[14] H.-O. Park, J. M. Bricker, M. J. Roy, J. E. Butler, Rheology of oscillating suspensions of noncolloidal spheres at small and large accumulated strains, Physics of Fluids 23 (1) (2011) 013302.

[15] D. Leighton, A. Acrivos, The shear-induced migration of particles in concentrated suspensions, Journal of Fluid Mechanics 181 (1987) 415–439.

[16] A. W. Chow, S. W. Sinton, J. H. Iwamiya, T. S. Stephens, Shear-induced particle migration in couette and parallel-plate viscometers : NMR imaging and stress measurements, Physics of Fluids 6 (8) (1994) 2561–2576.

[17] A. Acrivos, R. Mauri, X. Fan, Shear-induced resuspension in a couette device, International journal of multiphase flow 19 (5) (1993) 797–802.

[18] B. Saint-Michel, S. Manneville, S. Meeker, G. Ovarlez, H. Bodiguel, X-ray radiography of viscous resuspension, Physics of Fluids 31 (10) (2019) 103301.

[19] E. d'Ambrosio, F. Blanc, E. Lemaire, Viscous resuspension of non-Brownian particles : determination of the concentration profiles and particle normal stresses, Journal of Fluid Mechanics 911.

[20] I. Rampall, J. R. Smart, D. T. Leighton, The influence of surface roughness on the particle-pair distribution function of dilute suspensions of non-colloidal spheres in simple shear flow, Journal of Fluid Mechanics 339 (1997) 1–24.

[21] F. Blanc, F. Peters, E. Lemaire, Experimental signature of the pair trajectories of rough spheres in the shear-induced microstructure in noncolloidal suspensions, Physical review letters 107 (20) (2011) 208302.

[22] P. Pham, B. Metzger, J. E. Butler, Particle dispersion in sheared suspensions : Crucial role of solid-solid contacts, Physics of Fluids 27 (5) (2015) 051701.

[23] D. J. Pine, J. P. Gollub, J. F. Brady, A. M. Leshansky, Chaos and threshold for irreversibility in sheared suspensions, Nature 438 (7070) (2005) 997–1000.

[24] M. Maxey, Simulation methods for particulate flows and concentrated suspensions, Annual Review of Fluid Mechanics 49 (2017) 171–193.

[25] G. Bossis, J. F. Brady, Dynamic simulation of sheared suspensions. i. general method, The Journal of chemical physics 80 (10) (1984) 5141–5154.

[26] A. Sierou, J. Brady, Rheology and microstructure in concentrated noncolloidal suspensions, Journal of Rheology 46 (5) (2002) 1031–1056.

[27] R. Mari, R. Seto, J. F. Morris, M. M. Denn, Shear thickening, frictionless and frictional rheologies in non-Brownian suspensions, Journal of Rheology 58 (6) (2014) 1693–1724. doi :10.1122/1.4890747.

[28] S. Gallier, E. Lemaire, F. Peters, L. Lobry, Rheology of sheared suspensions of rough frictional particles, Journal of Fluid Mechanics 757 (2014) 514–549.

[29] R. Jackson, Locally averaged equations of motion for a mixture of identical spherical particles and a Newtonian fluid, Chemical Engineering Science 52 (15) (1997) 2457 – 2469, mathematical modelling of chemical and biochemical processes. doi :https ://doi.org/10.1016/S0009-2509(97)00065-1.

[30] R. Jackson, The dynamics of fluidized particles, Measurement Science & Technology 12 (2001) 755–755. doi :10.1088/0957-0233/12/6/701.

[31] M. Ouriemi, P. Aussillous, E. Guazzelli, Sediment dynamics. part 1. bed-load transport by laminar shearing flows, Journal of Fluid Mechanics 636 (2009) 295–319.

[32] R. Phillips, R. Armstrong, R. Brown, A. Graham, J. Abbott, A constitutive equation for concentrated suspensions that accounts for shear-induced particle migration, Physics of Fluids A 4 (1) (1992) 30–40.

[33] F. Boyer, É. Guazzelli, O. Pouliquen, Unifying suspension and granular rheology, Physical review letters 107 (18) (2011) 188301.

[34] W. Chèvremont, B. Chareyre, H. Bodiguel, Quantitative study of the rheology of frictional suspensions : Influence of friction coefficient in a large range of viscous numbers, Physical Review Fluids 4 (6) (2019) 064302.

[35] R. M. Miller, J. P. Singh, J. F. Morris, Suspension flow modeling for general geometries, Chemical Engineering Science 64 (22) (2009) 4597 – 4610, morton Denn Festschrift. doi :https ://doi.org/10.1016/j.ces.2009.04.033.

[36] J. F. Morris, A review of microstructure in concentrated suspensions and its implications for rheology and bulk flow, Rheologica acta 48 (8) (2009) 909–923.

[37] M. M. Denn, J. F. Morris, Rheology of non-Brownian suspensions, Annual review of chemical and biomolecular engineering 5 (2014) 203–228.

[38] R. N. Chacko, R. Mari, S. M. Fielding, M. E. Cates, Shear reversal in dense suspensions : The challenge to fabric evolution models from simulation data, Journal of Fluid Mechanics 847 (2018) 700–734.

[39] J. Gillissen, H. Wilson, Modeling sphere suspension microstructure and stress, Physical Review E 98 (3) (2018) 033119.

[40] O. Ozenda, P. Saramito, G. Chambon, Tensorial rheological model for concentrated non-colloidal suspensions : normal stress differences, Journal of Fluid Mechanics 898.

[41] J. T. Jenkins, R. Seto, L. La Ragione, Predictions of microstructure and stress in planar extensional flows of a dense viscous suspension, Journal of Fluid Mechanics 912.

[42] J. J. Gillissen, C. Ness, J. D. Peterson, H. J. Wilson, M. E. Cates, Constitutive model for time-dependent flows of shear-thickening suspensions, Physical review letters 123 (21) (2019) 214504.

[43] R. Seto, G. G. Giusteri, A. Martiniello, Microstructure and thickening of dense suspensions under extensional and shear flows, Journal of Fluid Mechanics 825.

[44] O. Cheal, C. Ness, Rheology of dense granular suspensions under extensional flow, Journal of Rheology 62 (2) (2018) 501–512. doi :10.1122/1.5004007.

[45] R. Bird, R. Armstrong, O. Hassager, Dynamics of polymeric liquids. Vol. 1 : Fluid mechanics, John Wiley and Sons Inc.,

New York, NY, 1987.

[46] R. I. Tanner, Engineering rheology, Vol. 52, OUP Oxford, 2000.

[47] G. Gupta, M. Massoudi, Flow of a generalized second grade fluid between heated plates, Acta Mechanica 99 (1) (1993) 21–33. doi :10.1007/BF01177232.
URL https://doi.org/10.1007/BF01177232

[48] M. Massoudi, T. Phuoc, The couette–poiseuille flow of a suspension modeled as a modified third-grade fluid, Archive of Applied Mechanics 86. doi :10.1007/s00419-015-1070-z.

[49] D. Lhuillier, Migration of rigid particles in non-Brownian viscous suspensions, Physics of Fluids 21 (2) (2009) 023302.

[50] A. Mahmud, S. Dai, R. I. Tanner, A quest for a model of non-colloidal suspensions with Newtonian matrices, Rheologica Acta 57 (1) (2018) 29–41.

[51] B. Andreotti, Y. Forterre, O. Pouliquen, Granular media : between fluid and solid, Cambridge University Press, 2013.

[52] J. Richardson, W. Zaki, Sedimentation and fluidisation : Part i, Trans. Inst. Chem. Eng 32 (1954) 35–53.

[53] M. Manninen, V. Taivassalo, S. Kallio, On the mixture model for multiphase flow, VTT Technical Research Centre of Finland, 1996.

[54] S. Márquez Damián, An extended mixture model for the simultaneous treatment of short and long scale interfaces, Ph.D. thesis, Universidad National del Litoral, Santa Fe, Argentina (03 2013).

[55] R. S. Rivlin, J. L. Ericksen, Stress deformation relation for isotropic materials, Indiana University Mathematics Journal 4 (1955) 323–425. doi :10.1512/iumj.1955.4.54011.

[56] N. Aksel, A brief note from the editor on the second-order fluid, Acta mechanica 157 (1-4) (2002) 235–236.

[57] H. Norem, F. Irgens, B. Schieldrop, A continuum model for calculating snow avalanche velocities, IAHS Publ 162 (1987) 363–379.

[58] W.-T. Wu, N. Aubry, J. Antaki, M. Massoudi, Flow of a dense suspension modeled as a modified second grade fluid, Fluids 3 (2018) 55. doi :10.3390/fluids3030055.

[59] W. O. Criminale, J. L. Ericksen, G. L. Filbey, Steady shear flow of non-Newtonian fluids, Archive for Rational Mechanics and Analysis 1 (1957) 410–417. doi :10.1007/BF00298018.

[60] P. Saramito, Complex fluids. Modeling and algorithms, Springer, 2016.

[61] P. Schunk, L. Scriven, Constitutive equation for modeling mixed extension and shear in polymer solution processing, Journal of rheology 34 (7) (1990) 1085–1119.

[62] R. I. Tanner, Aspects of non-colloidal suspension rheology, Physics of Fluids 30 (10) (2018) 101301.

[63] S. Dai, R. I. Tanner, Elongational flows of some non-colloidal suspensions, Rheologica Acta 56 (1) (2017) 63–71.

[64] R. I. Tanner, S. Dai, Particle roughness and rheology in noncolloidal suspensions, Journal of Rheology 60 (4) (2016) 809–818.

[65] R. Mari, R. Seto, Force transmission and the order parameter of shear thickening, Soft matter 15 (33) (2019) 6650–6659.

[66] C. Ness, J. Sun, Two-scale evolution during shear reversal in dense suspensions, Physical Review E 93 (1) (2016) 012604.

[67] G. L. Hand, A theory of anisotropic fluids, Journal of Fluid Mechanics 13 (1) (1962) 33–46.

[68] J. J. Stickel, R. J. Phillips, R. L. Powell, Application of a constitutive model for particulate suspensions : Time-dependent viscometric flows, Journal of Rheology 51 (6) (2007) 1271–1302.

[69] F. Blanc, E. Lemaire, F. Peters, Tunable fall velocity of a dense ball in oscillatory cross-sheared concentrated suspensions, Journal of Fluid Mechanics 746.

[70] J. M. Bricker, J. E. Butler, Correlation between stresses and microstructure in concentrated suspensions of non-Brownian spheres subject to unsteady shear flows, Journal of rheology 51 (4) (2007) 735–759.

[71] S. Athani, B. Metzger, Y. Forterre, R. Mari, Transient flows and migration in granular suspensions : key role of Reynolds-like dilatancy, arXiv preprint arXiv :2110.02342.

[72] H. Jasak, Error analysis and estimation for the finite volume method with applications to fluid flows, Ph.D. thesis, Imperial College London (1996).

[73] J. Ferziger, M. Peric, Computational Methods for Fluid Dynamics / J.H. Ferziger, M. Peric., Vol. 3, Springer-Verlag, 2002.

[74] F. Moukalled, L. Mangani, M. Darwish, The Finite Volume Method in Computational Fluid Dynamics : An Advanced Introduction with OpenFOAM® and Matlab®, Vol. 113, Springer, 2015. doi :10.1007/978-3-319-16874-6.

[75] T. Holzmann, Mathematics, Numerics, Derivations and OpenFOAM®, Tobias Holzmann, 2019.

[76] R. Miller, J. Morris, Normal stress-driven migration and axial development in pressure-driven flow of concentrated suspensions, Journal of Non-Newtonian Fluid Mechanics 135 (2006) 149–165. doi :10.1016/j.jnnfm.2005.11.009.

[77] M. Sarabian, M. Firouznia, B. Metzger, S. Hormozi, Fully developed and transient concentration profiles of particulate suspensions sheared in a cylindrical couette cell, Journal of Fluid Mechanics 862 (2019) 659–671.

[78] B. Snook, J. E. Butler, É. Guazzelli, Dynamics of shear-induced migration of spherical particles in oscillatory pipe flow, Journal of Fluid Mechanics 786 (2016) 128–153.

[79] K. Yeo, M. R. Maxey, Numerical simulations of concentrated suspensions of monodisperse particles in a poiseuille flow, Journal of fluid mechanics 682 (2011) 491–518.

[80] K. V. Deshpande, N. C. Shapley, Particle migration in oscillatory torsional flows of concentrated suspensions, Journal of

Rheology 54 (3) (2010) 663–686. doi :10.1122/1.3361668.

[81] A. Ramachandran, D. Leighton, Particle migration in concentrated suspensions undergoing squeeze flow, Journal of Rheology - J RHEOL 54. doi :10.1122/1.3372837.

[82] D. McCoy, M. Denn, Secondary flow in a parallel-disk viscometer, Rheologica Acta 10 (3) (1971) 408–411.

[83] T. Dbouk, Rheology of concentrated suspensions and shear-induced migration, Ph.D. thesis, Université Nice Sophia Antipolis (2011).

[84] J. M. Kim, S. G. Lee, C. Kim, Numerical simulations of particle migration in suspension flows : Frame-invariant formulation of curvature-induced migration, Journal of Non-Newtonian Fluid Mechanics 150 (2) (2008) 162 – 176. doi :https ://doi.org/10.1016/j.jnnfm.2007.10.012.

[85] B. K. Chapman, Shear-induced migration phenomena in concentrated suspensions, Ph.D. thesis, University of Notre Dame (1990).

[86] T. Moraczewski, H. Tang, N. Shapley, Flow of a concentrated suspension through an abrupt axisymmetric expansion measured by nuclear magnetic resonance imaging, Journal of Rheology 49 (2005) 1409–1428. doi :10.1122/1.2079227.

[87] E. Ryssel, P. Brunn, Comparison of a quasi-Newtonian fluid with a viscoelastic fluid in planar contraction flow, Journal of Non-Newtonian Fluid Mechanics 86 (3) (1999) 309–335. doi :https ://doi.org/10.1016/S0377-0257(99)00003-8.

[88] G. Zhong-Heng, T. Lehmann, L. Haoyun, C.-S. Man, Twirl tensors and the tensor equation, Journal of Elasticity 27 (1992) 227–245. doi :10.1007/BF00041688.

[89] P. Oliveira, F. Pinho, A. Schulte, A general correlation for the local loss coefficient in Newtonian axisymmetric sudden expansions, International Journal of Heat and Fluid Flow 19 (1998) 655–660. doi :10.1016/S0142-727X(98)10037-1.

[90] O. Ozenda, P. Saramito, G. Chambon, Shear-induced migration in concentrated suspensions : particle mass conservation, contact pressure and jamming, Journal of Non-Newtonian Fluid Mechanics 304 (2022) 104805.

[91] B. Lecampion, D. I. Garagash, Confined flow of suspensions modelled by a frictional rheology, Journal of Fluid Mechanics 759 (2014) 197–235.

[92] S. Oh, Y.-q. Song, D. I. Garagash, B. Lecampion, J. Desroches, Pressure-driven suspension flow near jamming, Physical review letters 114 (8) (2015) 088301.

[93] J. Morris, J. Brady, Pressure-driven flow of a suspension : buoyancy effects, International journal of multiphase flow 24 (1) (1998) 105–130.

[94] D. Monsorno, C. Varsakelis, M. Papalexandris, A two-phase thermomechanical theory for granular suspensions, Journal of Fluid Mechanics 808 (2016) 410–440.

[95] D. Monsorno, C. Varsakelis, M. Papalexandris, Poiseuille flow of dense non-colloidal suspensions : The role of intergranular and nonlocal stresses in particle migration, Journal of Non-Newtonian Fluid Mechanics 247 (2017) 229–238.